

PETROPHYSICAL PROPERTIES OF THE YESO, ABO AND CISCO FORMATIONS IN
THE PERMIAN BASIN IN NEW MEXICO, U.S.A

by

GRIFFIN MANN

Presented to the Faculty of the Graduate School of
The University of Texas at Arlington in Partial Fulfillment
of the Requirements
for the Degree of

MASTER OF SCIENCE IN GEOLOGY

THE UNIVERSITY OF TEXAS AT ARLINGTON

May 2017

Copyright © by Griffin Mann 2017

All Rights Reserved



Acknowledgements

I would like to thank CML Exploration for providing me with the samples and related data used to complete this research, as well as Highland (Texas) Energy for their ongoing support. I would also like to thank DrillingInfo for the consolidated data that I used throughout this study and Petra for providing a service capable of creating correlations and interpretations.

A special thanks goes out to my advisor Dr. Qinhong Hu for providing me with the guidance and direction throughout this process and my committee, Dr. John Wickham and Dr. Majie Fan for their support. I'd like to thank the University of Texas at Arlington and the rest of Dr. Hu's masters' students as well as PhD students for their help as well.

I'm grateful for the support that Truitt Matthews and Steve Burr of Highland (Texas) Energy have provided me throughout my time working with you. Last, but not least, I would like to thank my parents Nelson and Laurie Mann for always believing in me and my sisters for always being there for me.

May 24, 2017

Abstract

PETROPHYSICAL PROPERTIES OF THE YESO, ABO AND CISCO FORMATIONS IN THE PERMIAN BASIN IN NEW MEXICO, U.S.A

Griffin Mann, MS

The University of Texas at Arlington, 2017

Supervising Professor: Qinhong Hu

The area that comprises the Northwest Shelf in Lea Co., New Mexico has been heavily drilled over the past half century. The main target being shallow reservoirs within the Permian section (San Andres and Grayburg Formations). With a focus shifting towards deeper horizons, there is a need for more petrophysical data pertaining to these formations, which is the focus of this study through a variety of techniques.

This study involves the use of contact angle measurements, fluid imbibition tests, Mercury Injection Capillary Pressure (MICP) and log analysis to evaluate the nano-petrophysical properties of the Yeso, Abo and Cisco Formation within the Northwest Shelf area of southeast New Mexico. From contact angle measurements, all of the samples studied were found to be oil-wetting as n-decane spreads on to the rock surface much quicker than the other fluids (deionized water and API brine) tested. Imbibition tests resulted in a well-connected pore network being observed for all of the samples with the highest values of imbibition slopes being recorded for the Abo samples. MICP provided a variety of pore structure data which include porosity, pore-throat size distributions, permeability and tortuosity. The Abo samples saw the highest porosity percentages, which were above 15%, with all the other samples ranging from 4 – 7%. The majority of the pore-throat sizes for most of the samples fell within the 1 – 10 μm

range. The only exceptions to this being the Paddock Member within the Yeso Formation, which saw a higher percentage of larger pores (10 - 1000 μ m) and one of the Cisco Formation samples, which had the majority of its pore sizes fall in the 0.1 – 1 μ m range. The log analysis created log calculations and curves for cross-plot porosity and water saturation that were then used to derive a value for permeability. The porosity and permeability values were comparable with those measured from our MICP and literature values.

Table of Contents

Acknowledgements.....	iii
Abstract	iv
List of Illustrations	viii
List of Tables	x
Chapter 1 Introduction.....	11
Chapter 2 Geologic Setting and Depositional Environment.....	15
Permian Basin Geologic Setting	16
Northwest Shelf Geologic Setting	17
Well Log Interpretation	21
Chapter 3 Methods.....	28
Acquisition of Samples.....	28
Wettability / Contact Angle	35
Fluid Imbibition and Vapor Adsorption	36
Procedure.....	37
Mercury Injection Capillary Pressure (MICP).....	39
Procedure.....	42
Log Analysis.....	43
Water Saturation Calculation	44
Permeability from Porosity and Water Saturation.....	46
Chapter 4 Results	47
Wetting Characteristics	47
Pore Connectivity from Fluid Imbibition	52
Pore Connectivity from Vapor Adsorption.....	58

Pore Structure Characteristics from MICP Analyses	63
Porosity and Permeability from Log Analyses	68
Chapter 5 Discussion and Conclusion	74
Wettability.....	74
Pore Connectivity	74
Pore Structure Characteristics from MICP Analyses	75
Comparisons of Porosity and Permeability from Multiple Approaches	75
Conclusion	77
Recommendations	78
Appendix A Laboratory methods at Weatherford Laboratories.....	79
Appendix B Laboratory methods at Rotary Laboratories.....	81
References.....	83
Biographical Information	88

List of Illustrations

Figure 1-1 Study Area with basemap of wells	12
Figure 1-2 Stratigraphic Column Across Permian Basin.	13
Figure 2-1 Permian Basin Subdivisions	15
Figure 2-2 Cross-section depicting transition from Northwest Shelf to Delaware Basin ..	18
Figure 2-3 Producing wells in Permian Basin from Cisco Formation of Pennsylvanian age	19
Figure 2-4 Producing wells in Paddock, Blinberry and Abo sections of Permian age in Permian Basin	20
Figure 2-5 Structural cross-section A – A'	21
Figure 2-6 Map of cross-section A – A' with wells greater than 6,000 ft displayed	22
Figure 2-7 Type log of Paddy 18 State #2	24
Figure 2-8 Type log of the Gen Montcalm 25 State #1	25
Figure 2-9 Type log of the Abenaki 10 State #1.	27
Figure 3-1 Well locations with sample ID of cores taken from each well.....	29
Figure 3-2 Photos taken of samples upon arrival to the University of Texas at Arlington	32
Figure 3-3 Photo showing the Kino SL200KB apparatus used to measure contact angle.	36
Figure 3-4 Experimental apparatus and electric scale display (Shimadzu AUW 220D)...	38
Figure 3-5 Micrometric Autopore IV 9510 and Penetrometer filled with liquid mercury ..	43
Figure 3-6 Schlumberger tornado chart for estimating permeability from porosity and water saturation	46
Figure 4-1 Contact angle graphical results.	49
Figure 4-2 Yeso DI water imbibition results	55
Figure 4-3 Abo DI water imbibition results	56

Figure 4-4 Cisco DI water imbibition results	57
Figure 4-5 Yeso DI water vapor adsorption results	60
Figure 4-6 Abo DI water vapor adsorption results	61
Figure 4-7 Cisco DI water vapor adsorption result.	62
Figure 4-8 Abo 8956 D MICP example of inflection points	64
Figure 4-9 Graphical representation of pore size distribution results from MICP.....	67
Figure 4-10 Log analysis of Paddy 18 State #2 well with porosity and permeability comparisons.....	69
Figure 4-11 Log analysis of Gen Montcalm 25 State #1 well with porosity and permeability comparisons	70
Figure 4-12 Log analysis of Abenaki 10 State #1 well with porosity and permeability comparisons.....	71
Figure 4-13 Tornado chart showing the log derived permeability values for each sample	73
Figure 5-1 Paddy 18 State #2 perforations compared to Sw	76

List of Tables

Table 3-1 Samples used for study and previously measured data.....	31
Table 3-2 Sample Dimensions and weight upon arrival	32
Table 4-1 Results of contact angle measurements	48
Table 4-2 DI water imbibition slopes with the final slope averaged	53
Table 4-3 Vapor adsorption results utilizing DI water as the fluid.....	59
Table 4-4 Pore structure results obtained from MICP	66
Table 4-5 Pore size distribution results from MICP	67

Chapter 1

Introduction

The New Mexico portion of the Permian Basin consists of many producing formations that are produced both unconventionally as well as conventionally. Within the area that this study covers, the cored samples come from the Paddock and Blinberry intervals of the Yeso Formations, Abo and Cisco Formations, which are mainly carbonate reservoirs. The stacked pay, which is seen all across this area, provides favorable economics for oil and gas exploration and production. Understanding the petrophysical properties of each of these formations will provide a better understanding of how best to produce each formation and where they may be most productive.

This research study lies between two major oil fields, Vacuum on the east and Maljamar on the west (Figure 1-1). This area is located on the Northwest Shelf north of the Delaware Basin in Lea County, New Mexico. The Grayburg and San Andres Formations that have been targeted within these fields were discovered in the 1920's and 1930's. The Vacuum Field has produced roughly 342 million barrels of oil up to the year 2004, while the Grayburg-San Andres play within the Maljamar Field has produced roughly 158 million barrels of oil (Dutton et al., 2004). With these formations being heavily drilled for the past 80 years, many operators have begun to explore and produce deeper horizons within the Permian and Pennsylvanian sections. The results have varied as petrophysical characteristics such as porosity and permeability vary greatly throughout the area.

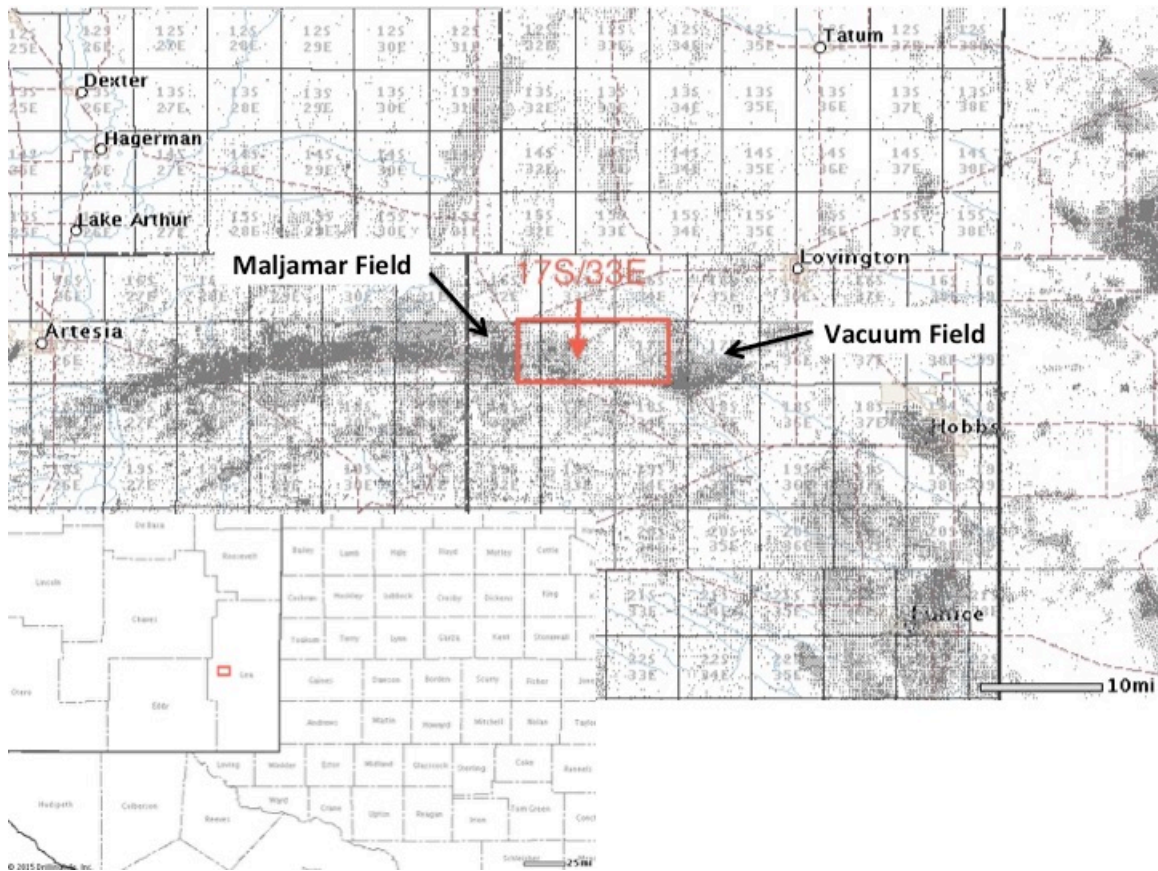


Figure 1-1. Study area with base map of wells (modified from Drilling-Info, 2017)

The Yeso Formation is made up of four members, known as the Paddock, Blinebry, Tubb and Lower Clearfork within the Permian section of the Northwest Shelf (Figure 1-2). The main productive ones of the Yeso are the Paddock and Blinebry Members, which are commonly produced together; in this work side wall cores were collected from the Paddock and Blinebry from the Paddy 18 State #2 well. Petrophysical properties vary with better porosity values ranging from 5 – 10% and permeability values ranging from 0.25 – 4 mD from helium pycnometry tests on core plugs (Weatherford Labs, 2008). Since 2013, horizontal Yeso wells have begun to be drilled and completed west of the area that this

study is focused on, but with mixed results (Drilling-Info, 2017).

System	Northwest Shelf		Delaware Basin		Midland Basin	
Permian		Dewey Lake		Dewey Lake		Dewey Lake
		Rustler		Rustler		Rustler
		Salado		Salado		Salado
				Castile		
	Whiten Horse	Tansill	Delaware Mountain Group	Lamar	Whitenhorse	Tansill
		Yates		Bell Canyon		Yates
		7 Rivers		Cherry Canyon		Seven Rivers
		Queen		Brushy Canyon		Queen
		Grayburg				Grayburg
	Word	San Andres	Bone Spring	Avalon Shale	Word	San Andres
		Glorieta		1st Bone Spring Sand		San Angelo
	Yeso	Paddock			Wolfberry / Wolffork	Clearfork
		Blaineberry		2nd Bone Spring Sand		Upper Spraberry
		Tubb				Lower Spraberry
		L. Clearfork		3rd Bone Spring Sand		Dean
		Abo		Wolfcamp		Wolfcamp
		Wolfcamp				
Pennsylvanian		Cisco		Cisco		Cisco
		Canyon		Canyon		Canyon
		Strawn		Strawn		Strawn
		Atoka		Atoka		Atoka
		Morrow		Morrow		

Figure 1-2. Stratigraphic columns across Permian basin with sample intervals highlighted for this work (Murchison, 2010)

The Abo Formation lies directly below the Yeso and is found to be a carbonate reservoir in most areas across New Mexico. To the south of the focus area for this study, the Abo is produced along a trend of a barrier reef that was formed on the edge of the Northwest Shelf and to the west from shallow shelf deposits (Broadhead and Speer, 1993). The Abo Formation has become a successful horizontal target within the Vacuum Field east of the study area, where it is found as a shallow shelf dolomite. In this study, side wall cores were taken in the Abo from the Gen Montcalm 25 State #1 well with the

better porosity values ranging from 10 – 20% and permeability values ranging from 0.9 – 4.1 mD for core plugs (Rotary Laboratories, 2006).

The Cisco Formation is found in the upper part of the Pennsylvanian and is a carbonate reservoir, which is more wide spread as the Cisco is produced in Texas as well. Within the area surrounding Lea County, New Mexico, the Cisco Formation is generally produced from a biohermal shelf limestone (Carleton, 1977). Not many wells have targeted the Cisco as a horizontal target, as it is usually is produced secondary to other reservoirs deeper within the Pennsylvanian section and in the above Permian section. The side wall cores of Cisco collected for this study were taken from the Abenaki 10 State #1 well, one of which being a limestone sample and the other a sandstone. Between these samples, measured porosity values from core plugs range from 8.5 – 10.2% and permeability ranges from 0.43 – 1.69 mD (Weatherford Labs, 2010).

This work will highlight the importance of wettability, pore size distribution, pore connectivity and tortuosity, as these petrophysical characteristics allow for an overall better understanding of these formations and improve the way in which they are explored for and produced. Advances in hydraulic fracturing have also improved the recovery factor of many of these reservoirs and has changed the way many of these formations are completed. The results gathered from this research will help determine what factors and characteristics are important in determining how to complete wells within these intervals and what makes them productive and economic or not.

Chapter 2

Geologic Setting and Depositional Environment

Located just north of the Delaware Basin, the Northwest Shelf is part of the greater Permian Basin (Figure 2-1). The entirety of the Permian Basin experienced a variety of depositional environments and tectonic changes throughout its history. The depositional environments and geologic setup of the region dating back to before the Mississippian provided favorable conditions for hydrocarbon generation and oil and gas entrapment all across west Texas and southeast New Mexico.

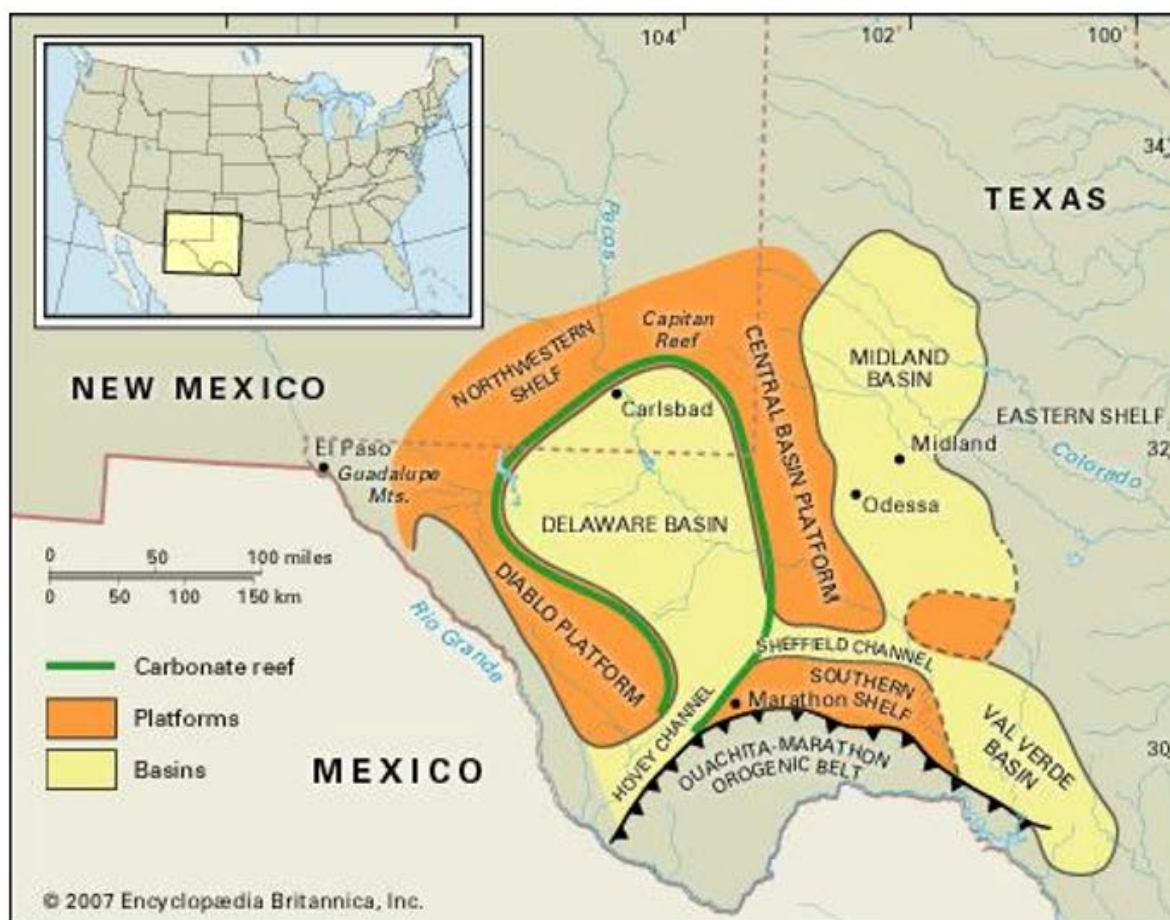


Figure 2-1. Permian Basin subdivisions (Encyclopedia Britannica, 2007)

Permian Basin Geologic Setting

During the Ordovician, Silurian and Devonian time periods, carbonate deposition was most common across the Permian Basin. These carbonate deposits were a result of a marine environment as a shallow sea could have encompassed most of the area (Galley, 1955). The Permian Basin during the Ordovician was located on the southwest edge of the Laurentia plate, with a shallow water shelf encompassing the Texas part of the area and a deeper water environment becoming prevalent as you move south (Loucks, 2008). The Ellenburger Formation, being a shallow water carbonate platform sequence, is a highly active oil and gas reservoir that is being produced all across the Delaware Basin and Midland Basin in west Texas. Across this same area during the Silurian, the Fusselman Formation is the main oil and gas reservoir, which was deposited in a similar depositional environment as it is considered to be a shallow water carbonate. During the Devonian, the main geologic formation that was deposited throughout the Permian Basin was the organic rich Woodford Shale. The depositional environment is consistent with a eustatic sea-level fall as terrestrial terrain took over much of the area (Hemmesch et al., 2014)

Mississippian strata consist mainly of limestone and shale, which could be the possible source rock for many reservoirs (Galley, 1955). The Barnett Formation, which is predominately shale, is the main formation deposited throughout the Permian Basin. The Barnett Formation represents a time of an overall relative sea level rise throughout the Permian Basin (Ruppel and Kane, 2006). The Barnett Shale is considered to be a source rock and has been successfully drilled in Fort Worth Basin due to the advances in drilling and completion technologies; few wells, however, have targeted this formation within the Permian Basin.

The tectonic environment changed towards the end of the Mississippian from an area of little to no relief to an almost enclosed basin surrounded by mountains of high relief (Galley, 1955). This change in tectonics is seen in the Pennsylvanian strata as

integrated marine shale, sandstone and limestone cover the Permian Basin dating back to this time period (Galley, 1955). Many oil and gas reservoirs are found in the Pennsylvanian system being trapped structurally and stratigraphically, which includes the Cisco Formation.

During the Permian a deep restricted marine basin covered the area known today as the Permian Basin. Clastic deposition dominated the marine area with thick carbonate intervals accumulating on the edges as shoal platforms surrounded the deep sea (Galley, 1955). The Northwest Shelf, which contains many of these thick carbonate intervals, is an example of one of the surrounding shoal platforms that is found on the edge of the deep marine sea. The samples analyzed for this work were taken from wells drilled in this area.

Northwest Shelf Geologic Setting

As seen in Figure 2-1, the Northwest Shelf is located directly north of the Delaware Basin and structurally becomes higher as you come up out of the basin. Many formations have been targeted for oil and gas all across the Delaware Basin, and the Bone Spring Formation with multiple zones has seen an increased amount of activity with roughly 5,000 wells being drilled targeting that interval up to 2016. Moving from the Delaware Basin to the Northwest Shelf, the Bone Spring interval changes from a basin limestone to a shelf-margin dolomite and correlates to the Abo and Yeso Formations (Figure 2-2). The Cisco Formation, being Pennsylvanian in age, can be found all across the Midland Basin, Delaware Basin and Northwest Shelf. On the Northwest Shelf the Cisco Formation is being produced primarily as a shelf limestone.

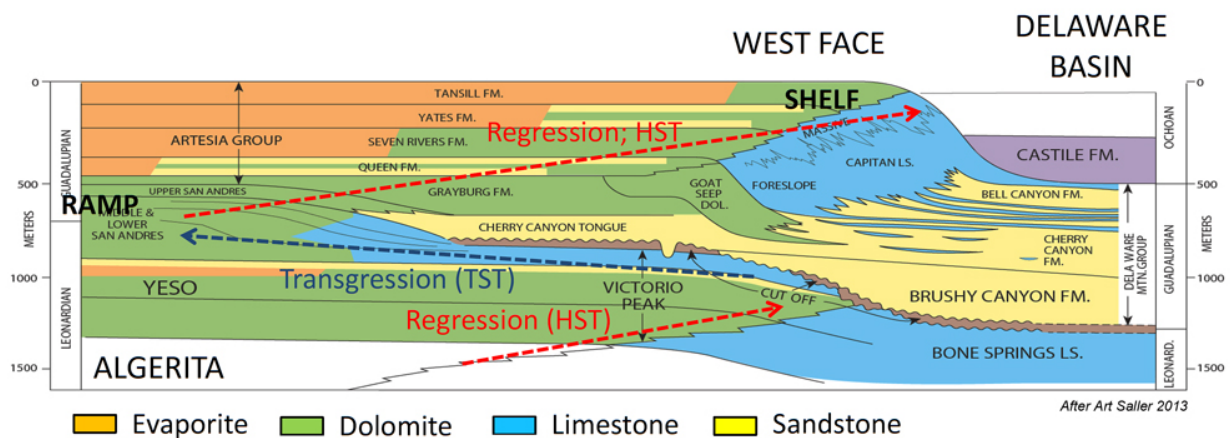


Figure 2-2. Cross-section depicting transition from Northwest Shelf to Delaware Basin.

HST: Highstand Systems Tract. TST: Transgressive Systems Tract (Saller, 2013)

During the Pennsylvanian period, the region comprised of west Texas and southeast New Mexico became an enclosed basin with areas of high relief surrounding the sides (Figure 2-3). The Central Basin Platform also becomes present during this time, separating the Delaware Basin on the west from the Midland Basin in the east. The Cisco has been produced both in the Midland Basin and Northwest Shelf.

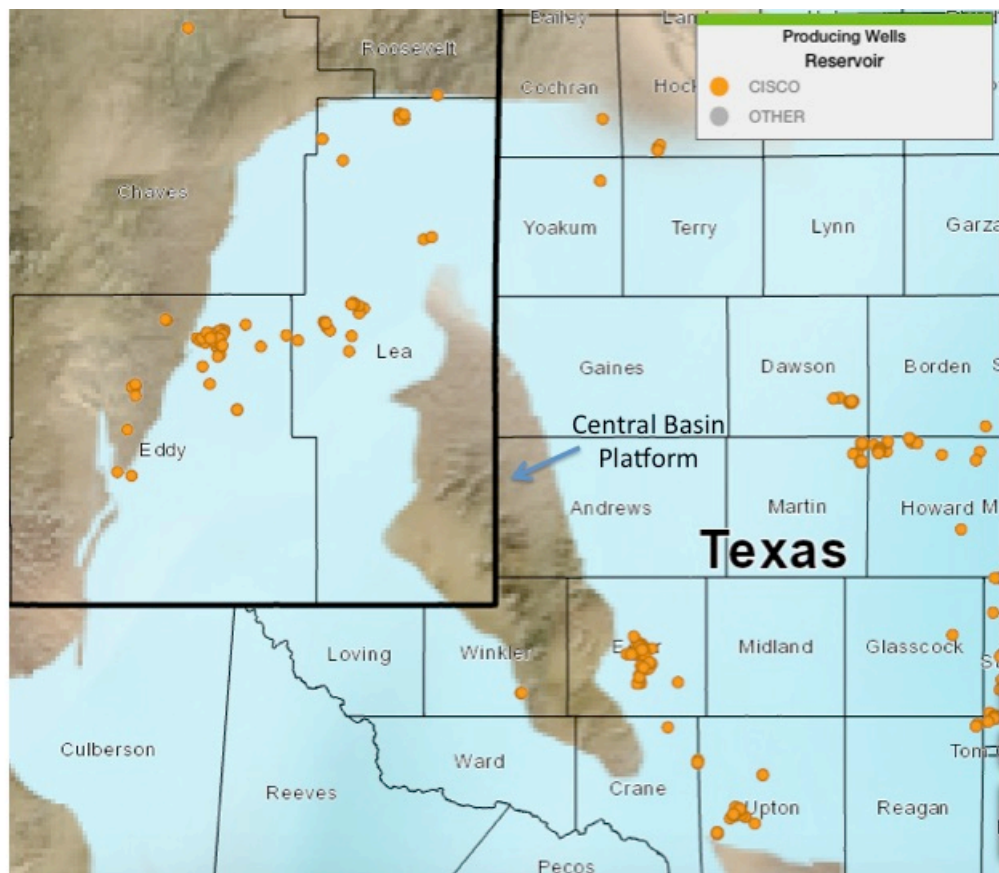


Figure 2-3. Producing wells in Permian Basin from Cisco Formation of Pennsylvanian age (plotted with Drilling-Info, 2017)

During the Permian, a deep marine basin encompasses the area known as the Delaware Basin. The Central Basin Platform still separates the Delaware Basin from the Midland Basin and the Northwest Shelf begins to take form as you come out of the deep marine sea. Stratigraphic differences are seen within the Permian as the Yeso Formation, which includes the Paddock and Blinberry Members, and the Abo Formation depositionally change as you move out of the Delaware Basin on to the Northwest Shelf. This is also seen in where these wells are located today targeting these formations as on the Northwest Shelf, reef and shelf deposits dominate the Permian stratigraphic intervals

(Figure 2-4).

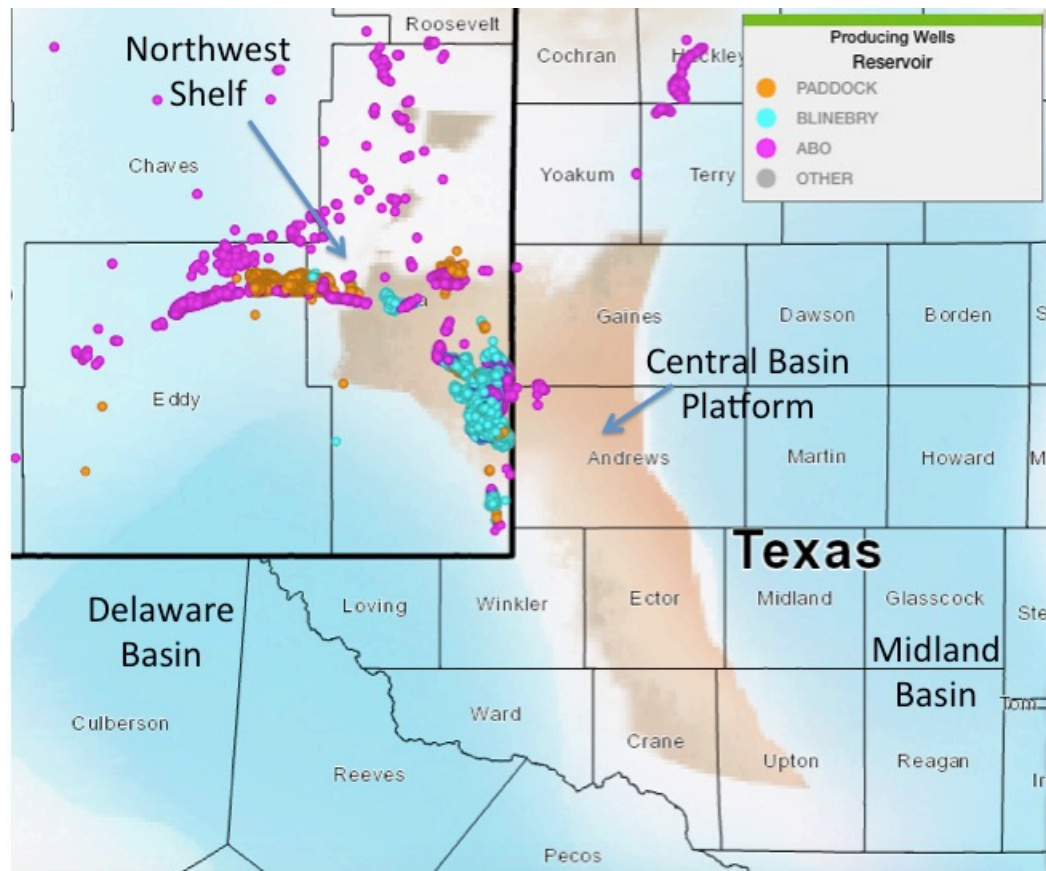


Figure 2-4. Producing wells in Paddock, Blinbry and Abo sections of Permian age in Permian Basin (plotted with Drilling-Info, 2017)

2-1 Well Log Interpretation

A variety of log types exist throughout this area in the form of digital logs as well as rasters. Figure 2-5 shows a structural cross-section starting in the Maljamar Field in the west and going through the area that the cores for the study were collected and ending in the Vacuum Field in the east. Most of the drilling activity in the past has been focused on the structurally higher areas which can be seen on both ends of the cross-section. This is also displayed in Figure 2-6, which shows a map of the wells greater than 6,000 ft and the location of the wells used for cross-section A – A'. There are however, structural variations within the lower area between the two fields that can contribute to how productive different areas can be.

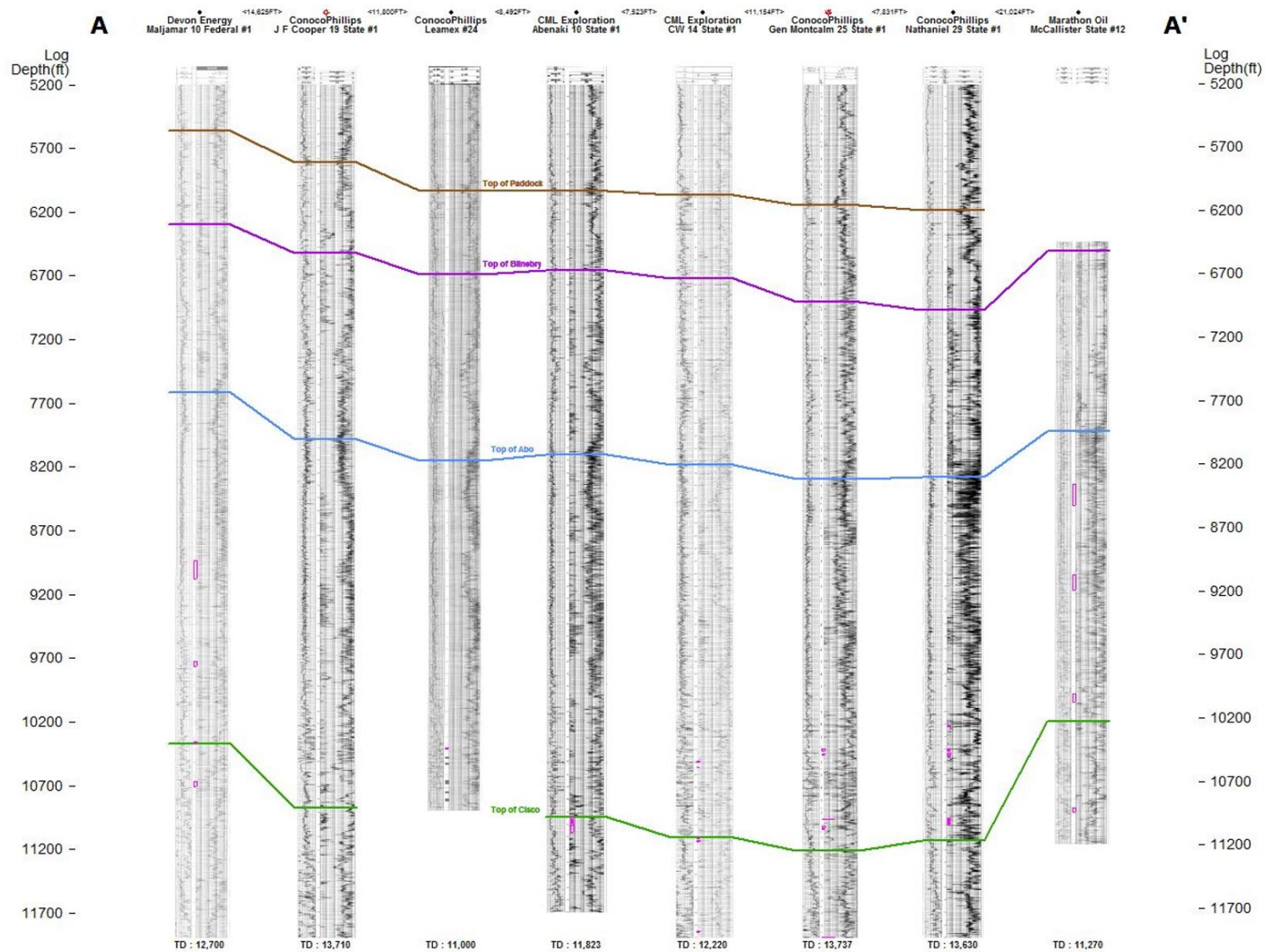


Figure 2-5. Structural cross-section A – A' (created in Petra)

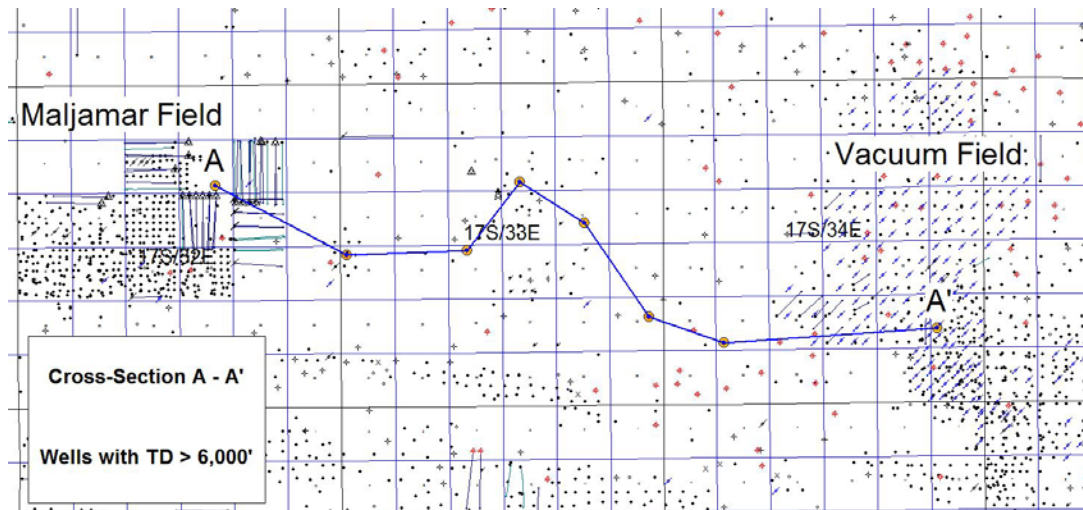


Figure 2-6. Map of cross-section A – A' with wells greater than 6,000 ft displayed.
(created in Petra)

Digital logs were used to give an in depth look at each formation being studied, and also to preform further log analyses. A type log was created for each of the three wells that the side-wall cores came from, which also shows where the tops were picked and gives us insight into the relative interval thicknesses of each formation. Figure 2-7 shows a type log from the Paddy 18 State #2 well, displaying the top of the Gloreitta, as well as the Paddock and Blinebry members of the Yeso Formation. The depths at which the side wall cores that were used for this study are marked by a black line and the perforated intervals are shown within the log track in purple.

CML Exploration Paddy 18 State #2

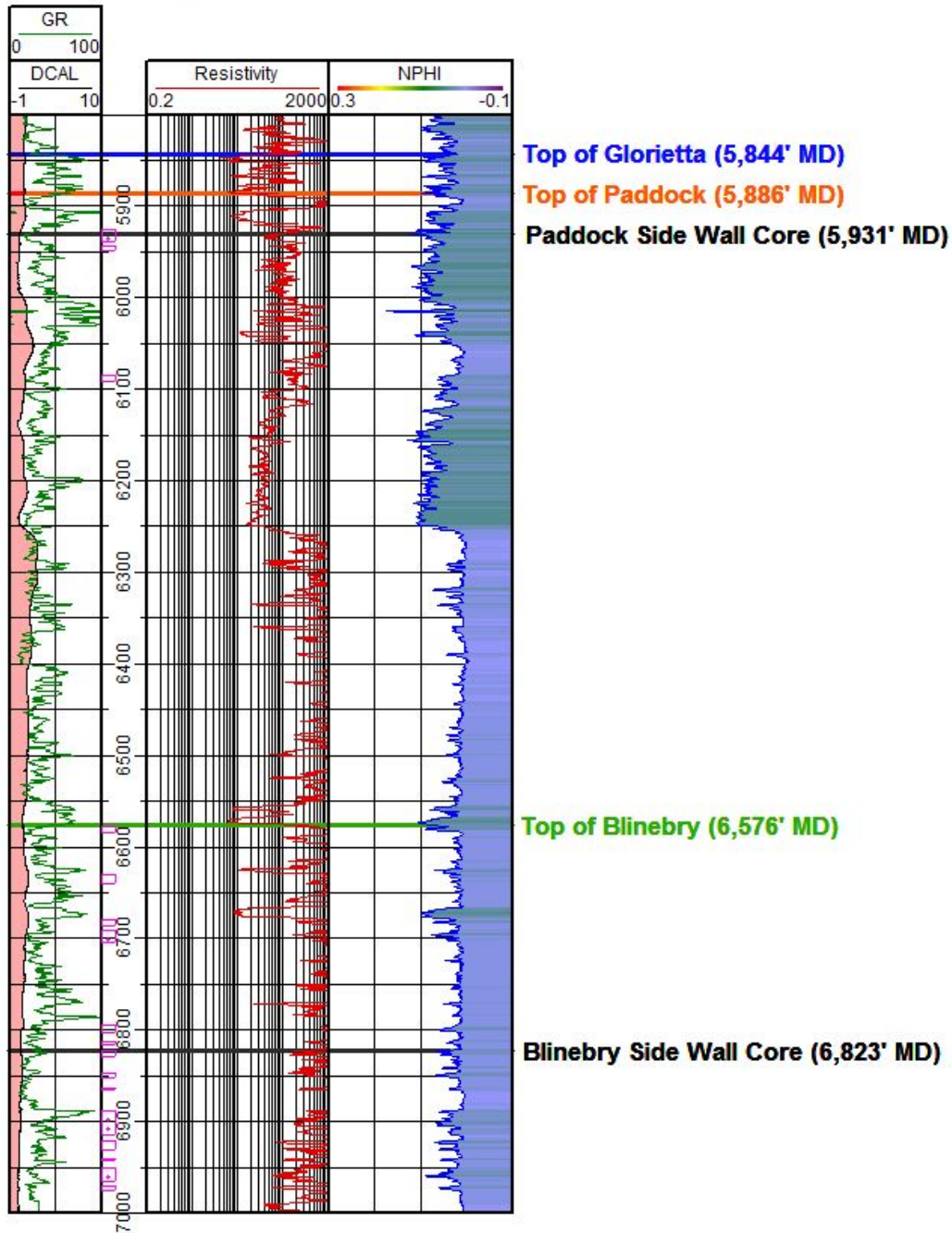


Figure 2-7. Type log of Paddy 18 State #2 (created in Petra)

Figure 2-8 is a type log from the Gen Montcalm 25 State #1 well, which shows part of the Abo interval. The top of the Abo is shown at a measured depth of 8,340 feet with another correlation marker designating the top of the pay interval seen in many of the Abo producing wells in the area.

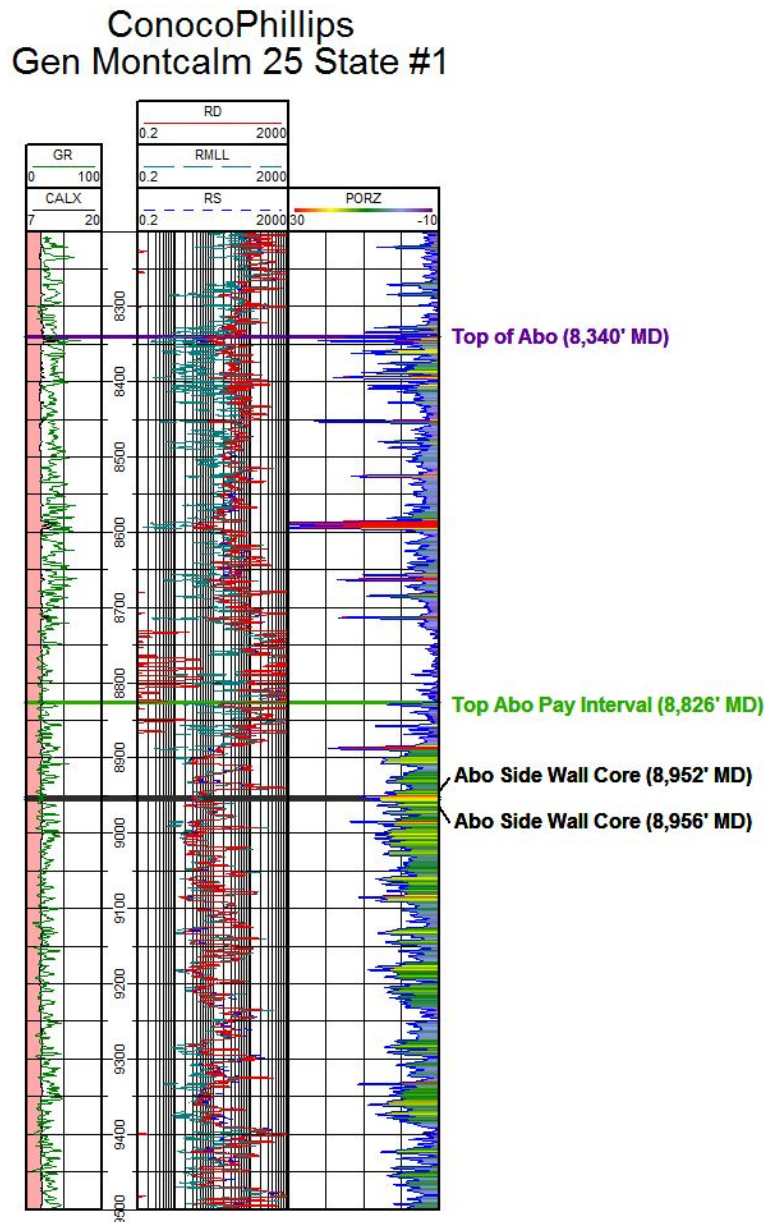
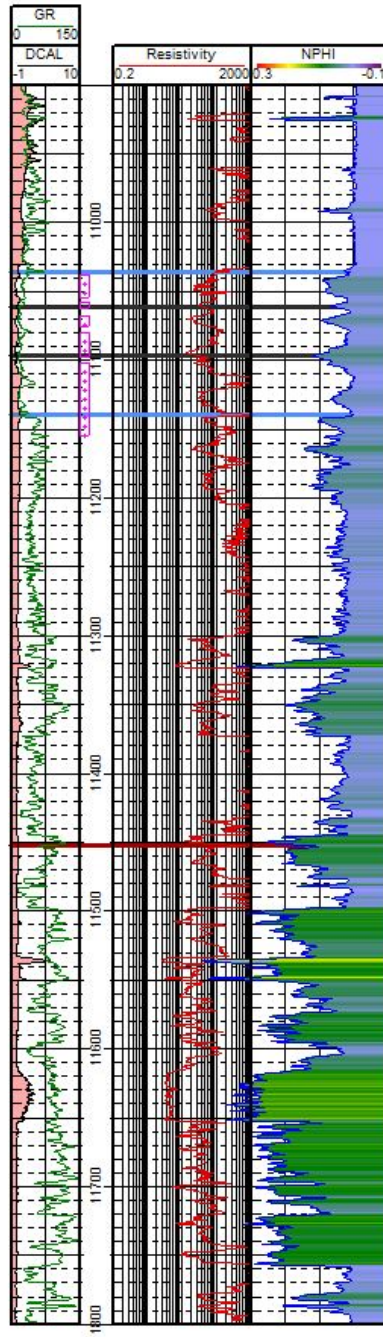


Figure 2-8. Type log of the Gen Montcalm 25 State #1 (created in Petra)

The type log for the Abenaki 10 State #1 well is shown in Figure 2-9 and displays part of the Cisco Formation. The top and base of the main producing interval of the Cisco is shown in blue with the top of the Cisco Clastics correlation marker shown in red. As you can see both of the side wall cores used in this study come from the currently producing zone shown from the perforated intervals.

CML Exploration
Abenaki 10 State #1



Top of Cisco (11,036' MD)

Cisco Side Wall Core (11,061' MD)

Cisco Side Wall Core (11,097' MD)

Base of Cisco (11,139' MD)

Top of Cisco Clastics (11,452' MD)

Figure 2-9. Type log of the Abenaki 10 State #1 (created in Petra)

Chapter 3

Methods

3-1 Acquisition of Samples

The samples that were used for this study came from three separate wells located in Lea Co., New Mexico (Figure 3-1), all of which being provided by CML Exploration in May of 2016. The Paddock and Blinbry sidewall cores came from the Paddy 18 State #2 well. The two Abo sidewall cores came from the Gen Montcalm 25 State #1 well, and the two Cisco sidewall cores came from the Abenaki 10 State #1 well. The depths at which these cores were taken are attached to the sample ID seen in the 1st column of Table 3-1. Weatherford Laboratories has performed routine lab work on the samples coming from the Paddy 18 State #2 well and the Abenaki 10 State #1 well (Appendix A). Rotary Laboratories performed the core analysis for the samples from the Gen Montcalm 25 State #1 well (Appendix B). Lithologic descriptions were noted by each laboratory that performed the initial analysis with all of the samples being described as dolomite with the exception of the Cisco samples; the Cisco 11061 LS sample was described as a limestone and the Cisco 11097 SS being sandstone. The data collected from these previous lab work are incorporated with the additional lab work performed at the University of Texas at Arlington, which is outlined below in this section. Along with core analyses, porosity and resistivity logs, acquired from the New Mexico Oil Conservation Division, are used to correlate the section and perform integrated data interpretation.

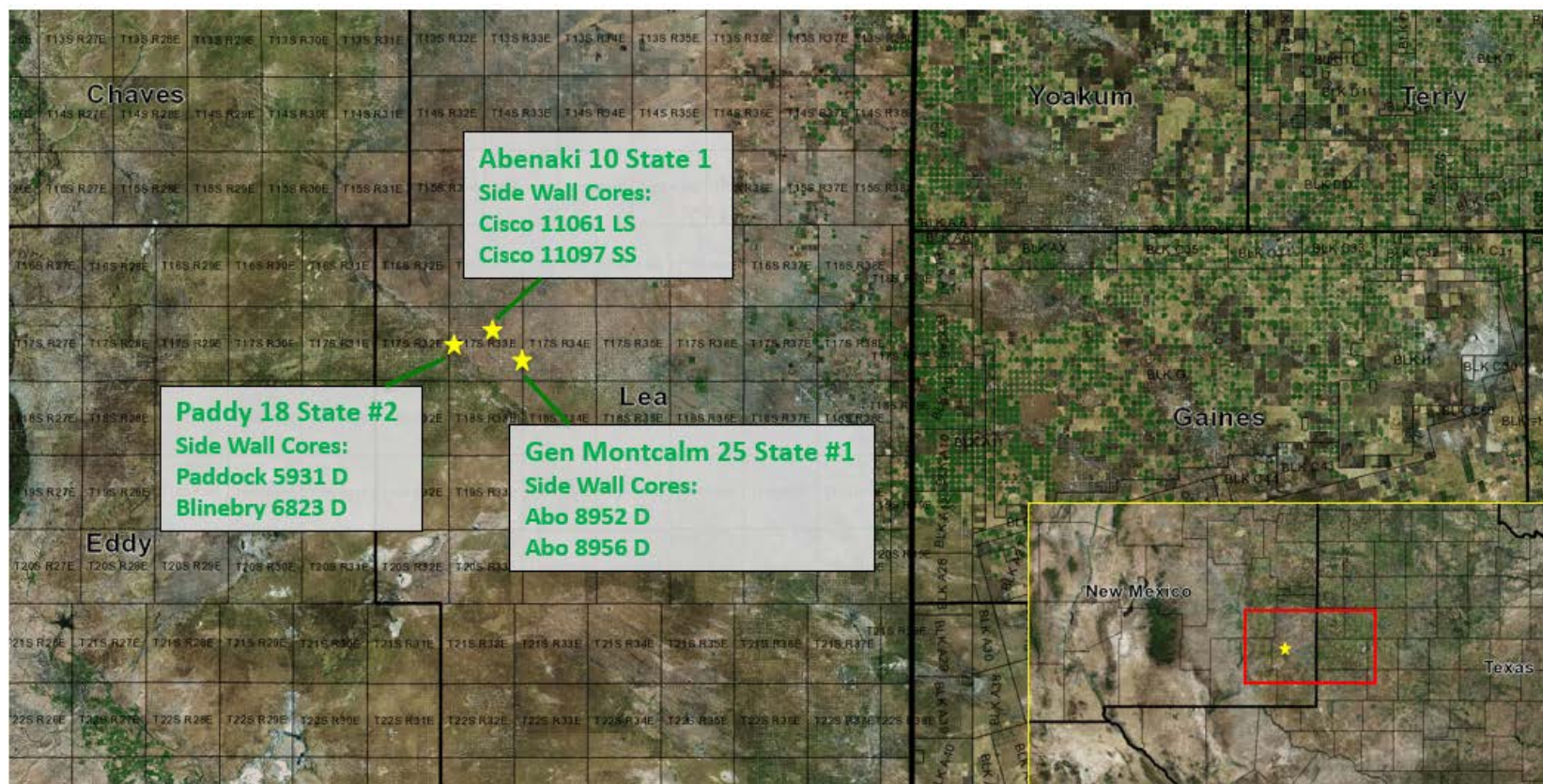


Figure 3-1. Well locations with sample ID of cores taken from each well.

Upon arrival all of the samples had their dimensions measured and mass weighed before being cut down in to the appropriate sizes required for the laboratory tests, which is seen in table 3-2. Along with that pictures were taken using a digital microscope camera before any work or cutting was performed (fig. 3-2). The (A) photos show a picture of the entire sidewall core. The (B) photos show a zoomed in picture of the sample.

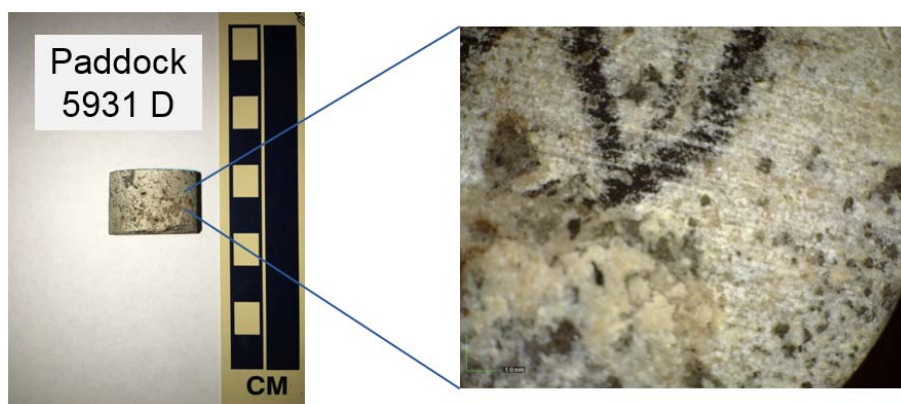
Table 3-1. Samples used for study and previously measured data

Sample ID	Well Name	Formation /Member	Grain Density (g/cm ³)	Porosity (%)	Permeability (mD)	Water Saturation (%)	Oil Saturation (%)	Gas Units	Fluorescence (%)
Paddock 5931 D	Paddy 18 State #2	Yeso/ Paddock	2.84	10.1	3.58	13.7	14.1	250	90
Bliebry 6823 D	Paddy 18 State #2	Yeso/ Bliebry	2.87	5.30	0.26	11.9	9.2	135	70
Abo 8952 D	Gen Montcalm 25 State #1	Abo	2.84	20.9	4.11	53.1	20.4	221	80
Abo 8956 D	Gen Montcalm 25 State #1	Abo	2.81	14.7	0.91	74.6	5.5	52	50
Cisco 11061 LS	Abenaki 10 State #1	Cisco	2.76	10.2	0.43	15.5	16.5	216	80
Cisco 11097 SS	Abenaki 10 State #1	Cisco	2.82	8.50	1.69	12.3	14.3	203	90

Weatherford Laboratories
Rotary Laboratories

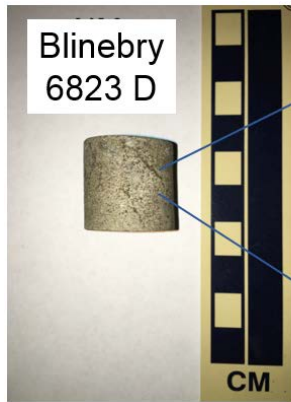
Table 3-2. Sample Dimensions and weight upon arrival

Sample ID	Diameter (cm)	Height (cm)	Weight (g)
Paddock 5931 D	2.331	1.598	16.6
Blinebry 6823 D	2.321	2.267	25.6
Abo 8952 D	2.536	3.457	36.1
Abo 8956 D	2.522	2.635	31.0
Cisco 11061 LS	2.345	1.820	18.8
Cisco 11097 SS	2.347	2.945	32.1



(A)

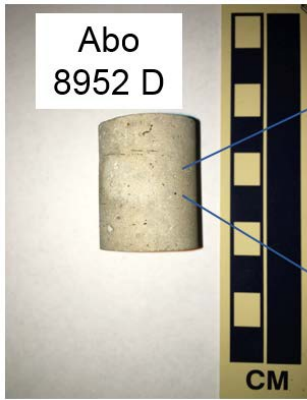
(B)



(A)



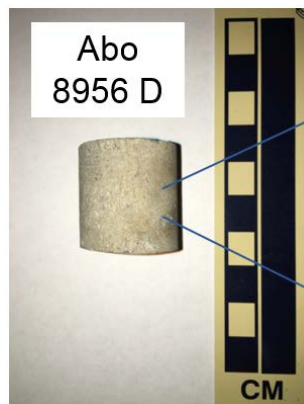
(B)



(A)



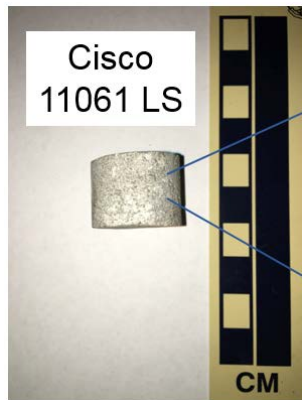
(B)



(A)



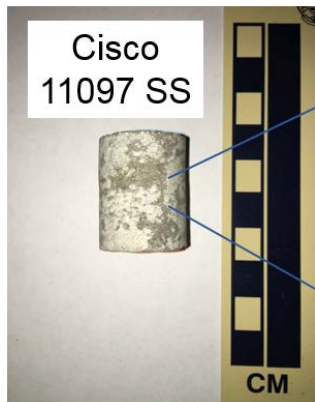
(B)



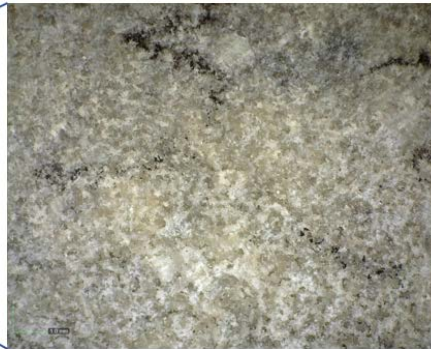
(A)



(B)



(A)



(B)

Figure 3-2. Photos taken of samples upon arrival to UTA.

In order to perform the necessary laboratory experiments, each of the samples were cut and polished into the required sizes to fully and judiciously utilize the sample mass. One to two roughly 1 cm cubes were cut for each sample. Three to four 2 mm x 10 mm x 10 mm slabs were cut for each of the six samples for the contact angle measurement. Epoxy was applied to 4 of the 6 sides leaving the top and bottom faces exposed for each of the cubes. The remaining fragments and cubes were then placed in a 60° C dry oven for 24 – 48 hrs. Once the samples were completely dry they were stored in a low humidity desiccator where they remained until testing.

3-2 Wettability / Contact Angle

Wettability is important to the primary, secondary, and tertiary recovery processes of hydrocarbons as it describes what type of fluid the producing formation or formation being studied prefers to spread onto or adhere to the rock surface (Teklu et al., 2015). Knowing the wetting preferences of a formation is key in determining recovery factors and deciding how to complete and fracture a well (Ma, 1994). For this study, each sample had three to four thin slabs cut and prepared for analyses using four different fluids (DI water, API brine, 10% or 20% IPA, and n-decane; API: American Petroleum Institute; IPA: isopropyl alcohol). The instrument used to perform the experiments is the Kino SL200KB shown in Figure 3-3. Each fluid was dropped onto the surface of the rock with the angle of contact being measured at different time intervals as the fluid spreads onto the rock surface. The more the fluid absorbs or spreads out onto the rock surface results in a lower recorded contact angle.

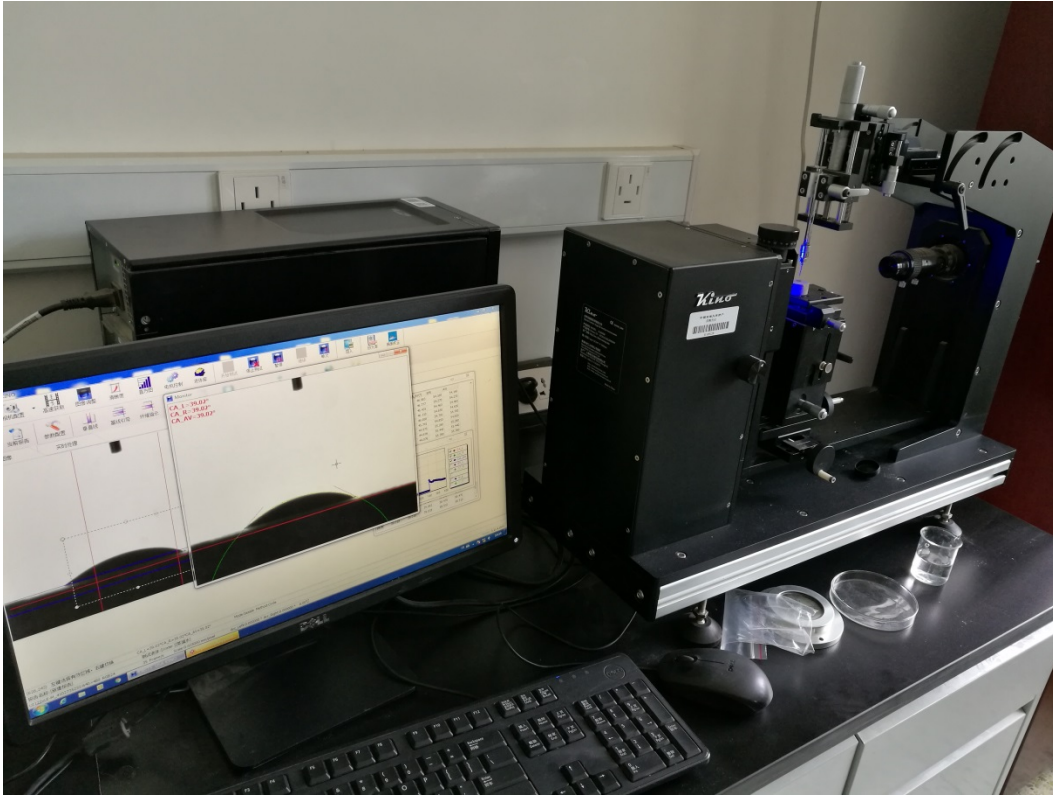


Figure 3-3. Photo showing the Kino SL200KB apparatus used to measure contact angle.

3-3 Fluid Imbibition and Vapor Adsorption

Imbibition tests are used to measure the amount of fluid uptake into porous rock over time. The results of each imbibition test will give us a better understanding of the pore connectivity and interactions of the different fluids on each sample. The factors that control the rate at which the fluid is imbibed include the sample porosity, wetting fluid and capillary pressure (Buckley and Leverett, 1941). There are two types of fluid imbibition; forced imbibition and spontaneous imbibition. Forced imbibition occurs when an external force is applied which generates the displacement, where spontaneous imbibition is the process of fluid penetrating the porous media due to capillary forces (mostly) and/or

gravity (Lopez and Soria, 2007). Spontaneous imbibition was used for this study using DI water and n-decane as the imbibing fluids. Pore connectivity is estimated using the slope of log imbibed liquid mass on the y-axis versus log time on the x-axis (Hu et al., 2012; Chukwama, 2015). Higher slopes upwards of 0.5 are generally recorded at the beginning of the tests as edge accessible porosity is a factor when the sample first comes in contact with the fluid. The slope decreases as the test continues due to the fluid only moving through the interior connected pore space. When the fluid reaches the top of the sample the slope will become almost horizontal.

Procedure for Fluid Imbibition and Vapor Adsorption Tests

This section will detail the methods and procedures used to perform the fluid imbibition and vapor adsorption tests. First, each of the samples was oven dried at 60° C for a time of 24 to 48 hours. They were then placed in a desiccator for a minimum of 10 minutes to keep a consistent humidity. While cooling, a petri dish (14.64 cm in diameter and 1.90 cm tall) was filled half full with the testing fluid (DI water or n-decane). The petri dish is then weighed with the mass being recorded and put inside the enclosed chamber beneath the analytical balance. The experimental setup can be seen in Figure 3-4. For water imbibition tests two cups of water are kept inside the enclosed chamber to keep the humidity constant throughout the lab test. The Shimadzu AUW 220D is the analytical balance used to keep track of the weight change throughout the experiment and sends that data to an Excel file periodically throughout the test. There is a hook attached to the bottom of the balance that attaches to a holder that securely holds the sample in place. The adjustable jack allows the chamber to move in the vertical direction so that the sample can come in to contact with the fluid.

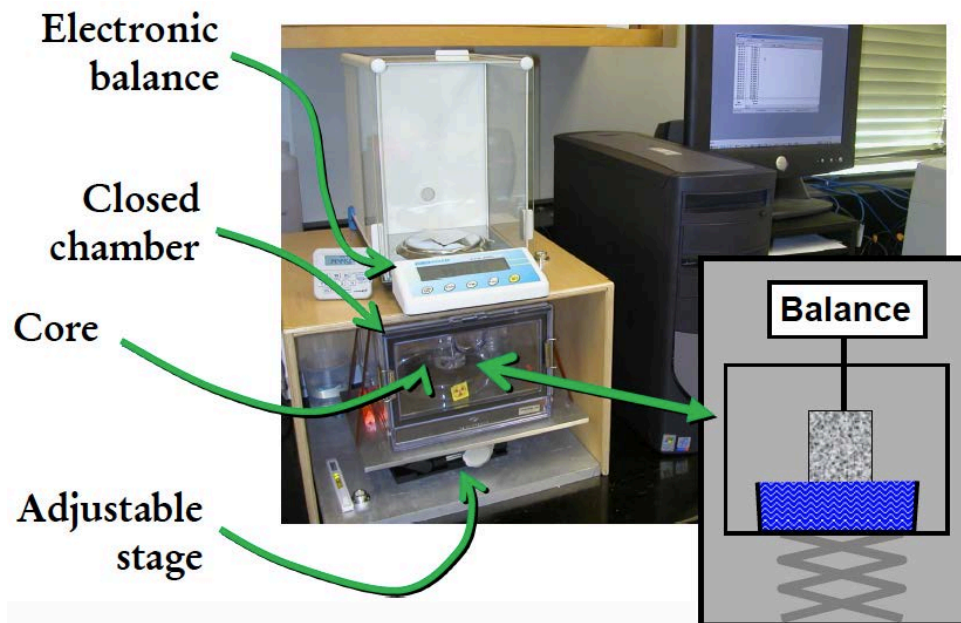


Figure 3-4. Experimental apparatus of imbibition tests

Once the petri dish with the fluid has been weighed and placed in to the closed chamber, the sample and holder are weighed and recorded separately. Then the sample is attached to the holder and they are both weighed and recorded as a single piece. The holder containing the sample is then placed on the hook attached below the analytical balance and the door is closed to the chamber. Once the hook is hanging in a still position and the weight has leveled off, the adjustable jack is raised to where it comes in contact with the flat surface of the sample hanging from the hook for all fluid imbibition tests. Vapor adsorption tests are set up the same way with the only difference being the sample hanging 2-4 cm above the fluid. Fluid imbibition tests using DI water as the fluid were run over three time periods of 6 hours, 12 hours and 24 hours. Fluid imbibition tests

using n-decane as the fluid was run over a time period of 8 hours. As for vapor adsorption tests, DI water runs lasted 3 days and n-decane runs lasted 2 days.

During the test the balance sent data to a computer at different interval times so that the weight could be recorded throughout the experiment. For the first 2 minutes the scale sent data over every 1 second. For the next hour it sent data over every 30 seconds. Then for 5 hours the interval time was set at 2 minutes and then changed to 5 minutes after the 6 hour mark for the remainder of the test. Once the test has completed the holder and sample are removed from the hook for the final weight to be measured and recorded. A moist kimwipe is weighed before doing this and then wiped across the exposed face of the sample to remove any residual fluid that is adhered to the sample surface. The kimwipe is then weighed again to measure the weight after wiping has occurred. The sample plus holder are then weighed and recorded as a single piece and then removed from each other to get a final sample and holder weight. The petri dish is now removed from the chamber and weighed to measure the amount of fluid loss compared to the initial weight of the dish before the test began. The data collected is then processed and results reviewed for further analysis and conclusions to be made.

3-3 Mercury Injection Capillary Pressure (MICP)

Mercury injection capillary pressure (MICP) is used to measure pore structure characteristics such as total pore area, bulk density, porosity, pore throat distribution, permeability and tortuosity. The results of this test will give us a better understanding of the pore size distribution, connectivity and other important factors that affect fluid flow and productivity of each formation. Liquid mercury, which has a high surface energy and is nonwetting is used to immerse each sample and invade the pore throats (Hu et al., 2015). As pressure increases, smaller pore throats can be invaded. Since mercury is

nonwetting, it will only invade pores once an external pressure is applied with the diameter of the pores being inversely proportional to the applied pressure (Gao and Hu, 2013). This is expressed through the Washburn equation assuming that the geometry of all pores are cylindrical in shape (Washburn, 1921).

Equation 3.1 expresses the inversely proportional relationship between pore diameters and the applied pressure.

$$\Delta P = -\left(\frac{2\gamma\cos\theta}{r}\right) \dots\dots\dots(3.1)$$

Where,

ΔP – Difference in pressure (psia);

γ – Surface tension for mercury (dynes/cm);

θ – Contact angle between porous media and mercury (degrees);

r – Corresponding pore throat radius (μm)

The original Washburn equation doesn't account for varying contact angle and surface tension values and has since been modified through the work of Wang et al. (2016). Wang's modified Washburn equation takes in to account for these varying values, which is especially important when the pore throat diameter falls below 10 nm. Equation 3.2 shows the modified Washburn equation outlined in the Wang et al. (2016) paper.

$$\Delta P = -\left(\frac{2\gamma Hg(r)\cdot\cos\theta Hg(r)}{r}\right) \dots\dots\dots(3.2)$$

Values for permeability can be calculated from MICP using the applied pressure and intrusion volume collected throughout the experiment (Quintero, 2016). The Katz and Thompson equation (1986; 1987) outlines how permeability is derived with.

Equation 3.3 from MICP data.

$$K = \left(\frac{1}{89}\right)(L_{max})^2 \left(\frac{L_{max}}{L_c}\right) \Phi S(L_{max}) \dots\dots\dots(3.3)$$

Where,

K – Absolute permeability (μm^2);

L_{max} - Pore throat diameter when hydraulic conductance is at its maximum (μm);

L_c – Length of the pore throat diameter (μm) corresponding to the threshold pressure, which is taken from the inflection point of the cumulative intrusion curve;

Φ – Porosity of the sample (%);

$S(L_{max})$ – represents the saturation at L_{max} (Gao and Hu, 2013)

Another important characteristic that affects pore connectivity and fluid migration is tortuosity, which can be empirically derived using direct measurements from MICP (Hu et al., 2015).

Equation 3.4 shows how tortuosity is derived from MICP data (Hager, 1998; Webb, 2001)

$$\tau = \sqrt{\frac{\rho}{24k(1 + \rho V_{tot})} \int_{\eta=r_{c,min}}^{\eta=r_{c,max}} \eta^2 f v(\eta) d\eta} \dots\dots\dots(3.4)$$

Where,

τ – Tortuosity (dimensionless);

ρ – Bulk density (g/cm^3);

V_{tot} – Total pore volume (mL/g);

$\int_{\eta=r_{c,min}}^{\eta=r_{c,max}} \eta^2 f v(\eta) d\eta$ - Pore throat volume probability density function.

Procedure for Mercury Intrusion Capillary Pressure (MICP)

Before beginning each MICP experiment, the samples are dried for 24-48 hrs in an oven to remove any fluid that may be occupying the pores and then placed in a desiccator that is set at room temperature to cool the sample. The samples were then cut down in to the appropriate sizes if needed and photos were taken to document the apparent geometries. The machine used to perform MICP analysis is the Micromeritics Autopore IV 9510 which is shown in Figure 3-5. A penetrometer (Figure 3-5), that is chosen according to the specific sample characteristics, is used to enclose the sample in a bulb and inject mercury into the sample. The sample weight (~2-3 g) is recorded along with the penetrometer, and the penetrometer plus the sample, and entered in to the computer under the analysis conditions before the low pressure analysis is performed. Once the appropriate filling pressures (0.5 or 5 psi, for sample porosities of 5-20%) and conditions are entered in to the computer the low pressure analysis is performed by injecting mercury into the bulb. Before liquid mercury is injected however, the sample is evacuated to 6.7 Pa (Hu et al., 2015). Liquid mercury then fills up the bulb and in some cases begins to invade the larger pores as the pressure increases throughout low pressure analysis. Once this is complete, the penetrometer is taken out of the low pressure compartment, weighed with the bulb filled with liquid mercury and placed in to the main compartment of the Micromeritics Autopore IV 9500 for the remainder of the experiment. The high pressure analysis conditions are then entered in to the computer and then the experiment resumes. The pressure increases to 60,000 psia (414 MPa) with the amount of intrusion being recorded compared to the applied pressure. The overall length of the experiment roughly takes 2 hrs to complete.

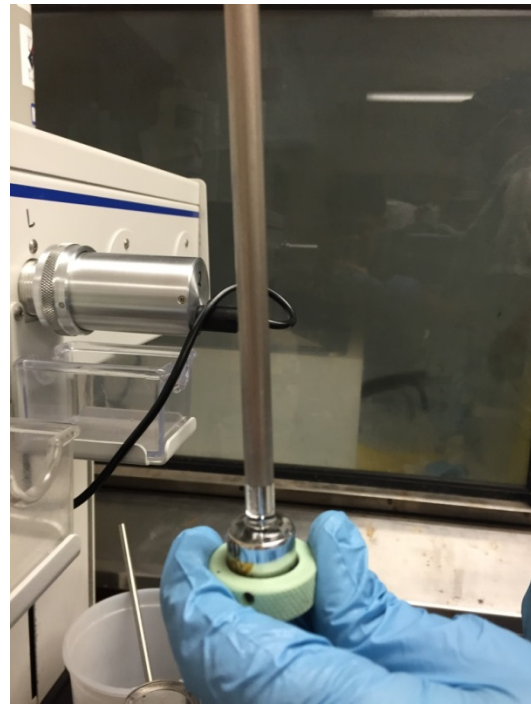


Figure 3-5. Micromeritics Autopore IV 9510 (left photo) and a penetrometer filled with liquid mercury (right photo)

3-4 Log Analysis

Log analysis can be used to provide numerous information about different properties of the rock and correlate between multiple wells. All of the raster logs used in this study were found in the New Mexico Oil Conservation Division (NMOCD) online library. The digital logs used to perform in-depth analyses for three study wells were provided by CML Exploration, LLC. The type logs seen in the Well Log Interpretation section were created using the general log runs from the logging company. Further calculations can be made based on those curves to provide more data pertaining to the petrophysical properties of each formation.

Water Saturation Calculation

Water saturation is an important calculation as it can provide insight into what type of fluid is occupying the pores. The higher the water saturation, the more likely the pores are filled with water and not hydrocarbons (Morris and Biggs, 1967). In order to create a curve for water saturation, different variables need to be obtained relating to Archie's Equation (Masoudi et al., 2011).

Equation 3.4 modified Archie's Equation for calculating water saturation (Masoudi et al., 2011)

$$S_w = \left(\frac{R_w}{R_t \times \phi^m} \right)^{\frac{1}{n}} \dots\dots\dots(3.4)$$

Where,

S_w – Water saturation (fraction);

R_w – Water resistivity (ohm m);

R_t – True resistivity (ohm m);

ϕ - Cross-plot porosity (%);

m – Cementation factor (dimensionless);

n – Saturation exponent (dimensionless).

Cross-plot porosity curves were available for all three wells used in this study, whereas true resistivity log curves were only available for the Paddy 18 State #2 and Abenaki 10 State #1 wells. For the Gen Montcalm 25 State #1 well the deep resistivity curve was used in place of the true resistivity to calculate for water saturation. Cementation and saturation exponents were both set at 2 as that is the average value used within this area.

Water resistivity (R_W) values require a separate calculation based off of water analysis tests from nearby wells within each given formation. The water analysis used for the Paddock and Blinebry Members came from the nearby Paddy 13 State #1 well, which was conducted by Martin Water Laboratories. The Abo water analysis used came from multiple wells within the Vacuum field and the Cisco water analysis came from the Leamex #9 well. Based on these tests, water resistivity at each reservoir depth can be computed using Equation 3.5.

Equation 3.5 shows the water resistivity temperature correction calculation (Doveton, 1999)

$$R_W = R_I \left(\frac{T_1 + 6.77}{T_2 + 6.77} \right) \dots \dots \dots (3.5)$$

Where,

R_W = Water resistivity (ohm-m);

R_I = Measured resistivity (ohm-m);

T_1 = Temperature at measured resistivity R_I (Fahrenheit);

T_2 = Reservoir temperature (Fahrenheit).

A water resistivity value of 0.044 was determined for the Paddock and Blinebry intervals, and used for calculating water saturation in the Paddy 18 State #2 well. A value of 0.038 was calculated for the Abo, which was used in water saturation calculations for the Gen Montcalm 25 State #1 well. The Cisco water resistivity calculation came out to be 0.075, which is used in the calculation of Abenaki 10 State #1 water saturation.

Permeability from Porosity and Water Saturation

Permeability can be estimated by plotting porosity against water saturation values for a given depth point. This is done by using a tornado chart created by the logging company (Schlumberger, 2009), which was developed for shales, sandstones and hydrocarbon-saturated intergranular rocks. Figure 3-6 shows the tornado chart used to estimate permeability for each of the depths at which the samples in this study were taken from. Water saturation is plotted on the x-axis whereas porosity is plotted on the y-axis.

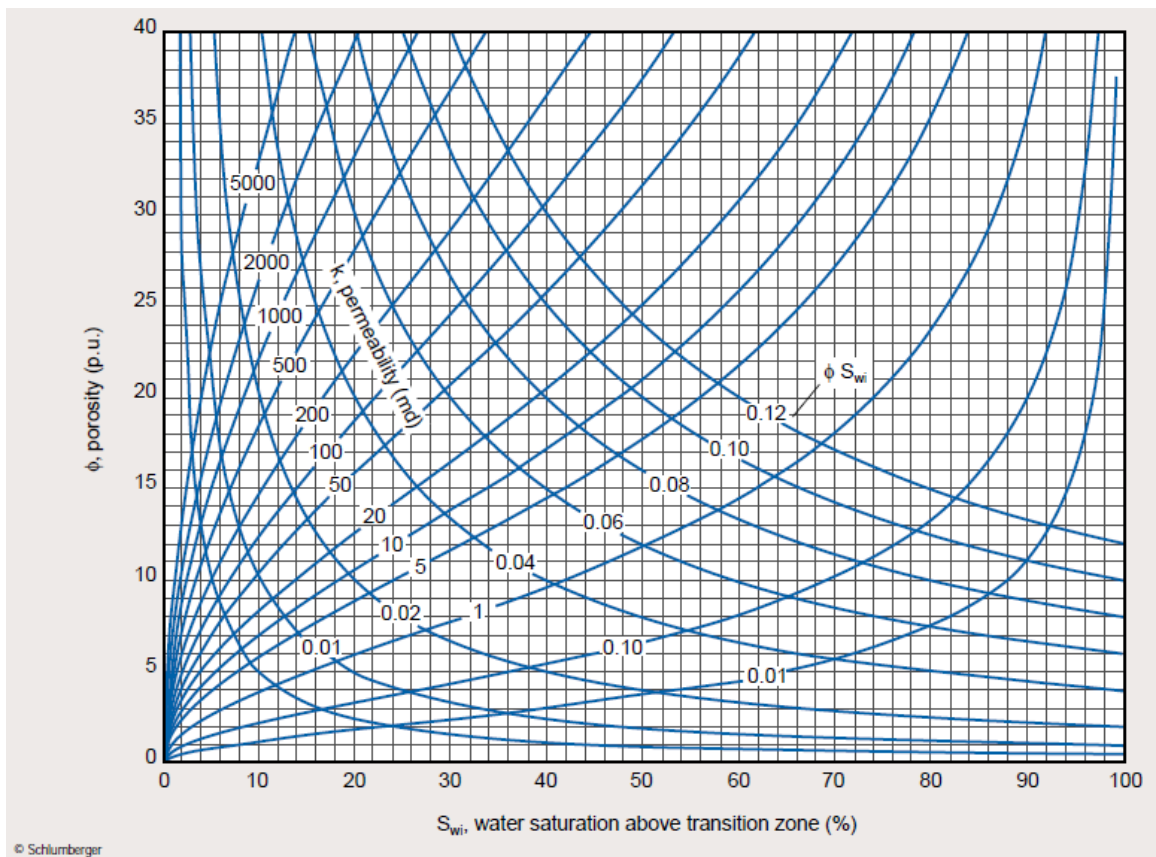


Figure 3-6. Schlumberger tornado chart for estimating permeability from porosity and water saturation (Schlumberger, 2009)

Chapter 4

Results

Wetting Characteristics

The four fluids that were tested on each sample were DI water, API brine, isopropyl alcohol (10% or 20% in water v/v) and n-decane. The results with associated fluid are shown in Table 4-1, with the contact angle measurement being taken at the 30 second mark of the experiment. The duration for some of the tests did not reach 30 seconds and is denoted by parenthesis; for these contact angle measurements in Table 4-1, the angles were taken from the last recorded point. A graphical representation for each sample (Figure 4-1) displays how quickly the contact angle decreased over the duration of the experiment. The contact angle in degrees is shown on the y-axis and the elapsed time in seconds is shown in a logarithmic scale on the x-axis with a red dashed line denoting the 30 second mark.

The results for each sample tell whether the sample surface is more hydrophobic or hydrophilic towards each fluid. Generally for hydrophobic fluids (DI water, API brine and 10% or 20% IPA), the contact angles were high as the fluids would create beads on the sample surfaces and either not absorb into the rock or do so very slowly. This indicates that the samples had a small extent of hydrophilic characteristic towards these fluids. There were some variations however between some of the studied samples. For instance, the Abo 8952 D sample had a much lower contact angle for all the fluids, especially DI water. Even though the n-decane fluid still had the lowest contact angle, this sample may contain more of a mixed-wetting characteristic in comparison to the other samples studied. The Cisco 11097 SS sample had a somewhat lower DI water contact angle and the lowest 10% IPA contact angle of the samples studied. This may

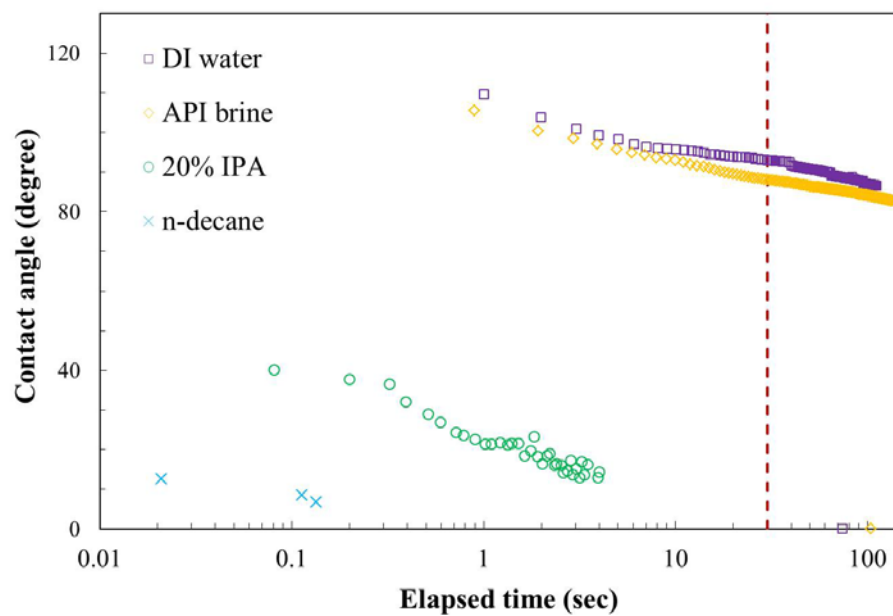
be due to the lithology of the rock being of sandstone in comparison to dolomite or limestone.

All of the samples displayed a hydrophobic characteristic towards n-decane as the sample surfaces almost completely absorbed the fluid and resulted in very low contact angles. From looking at Figure 4-1, all of the samples absorbed the n-decane fluid much quicker than any of the other fluids that were tested. This affinity towards n-decane indicates that each of the samples used in this study were preferably oil-wetting.

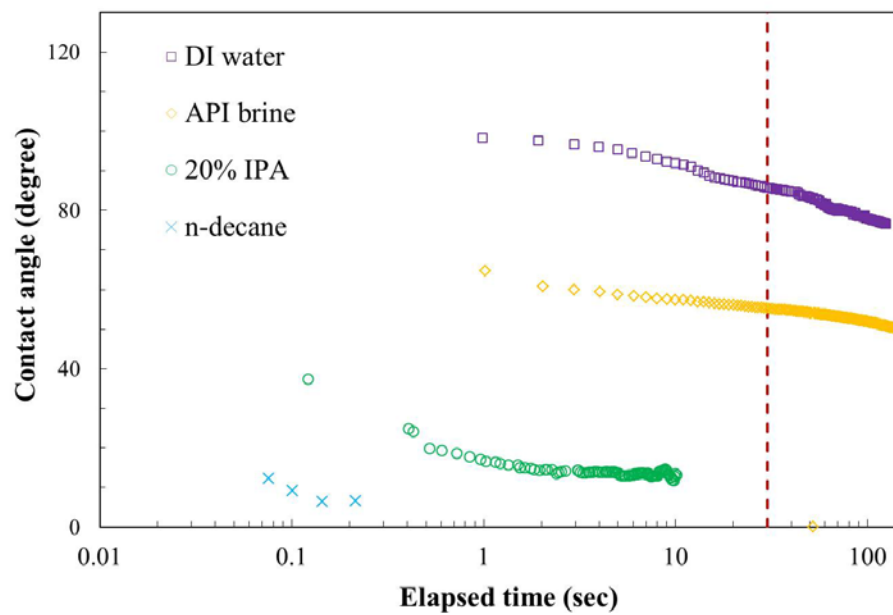
Table 4-1 Results of contact angle measurements

Sample ID	DI Water	API Brine	10% or 20% IPA	N-Decane
Paddock 5931 D	93.01°	88.12°	14.32° (4 sec)	6.86° (0.1 sec)
Blinebry 6823 D	85.70°	55.22°	13.23° (10 sec)	6.63° (0.2 sec)
Abo 8952 D	12.71°	18.69°	17.38° (17 sec)	<3° (0.8 sec)
Abo 8956 D	62.51°	80.48°	29.88°	6.26° (0.1 sec)
Cisco 11061 LS	42.30°	41.69°	34.99°	4.55° (0.01 sec)
Cisco 11097 SS	37.32°	60.82°	8.22° (22 sec)	5.72° (0.1 sec)

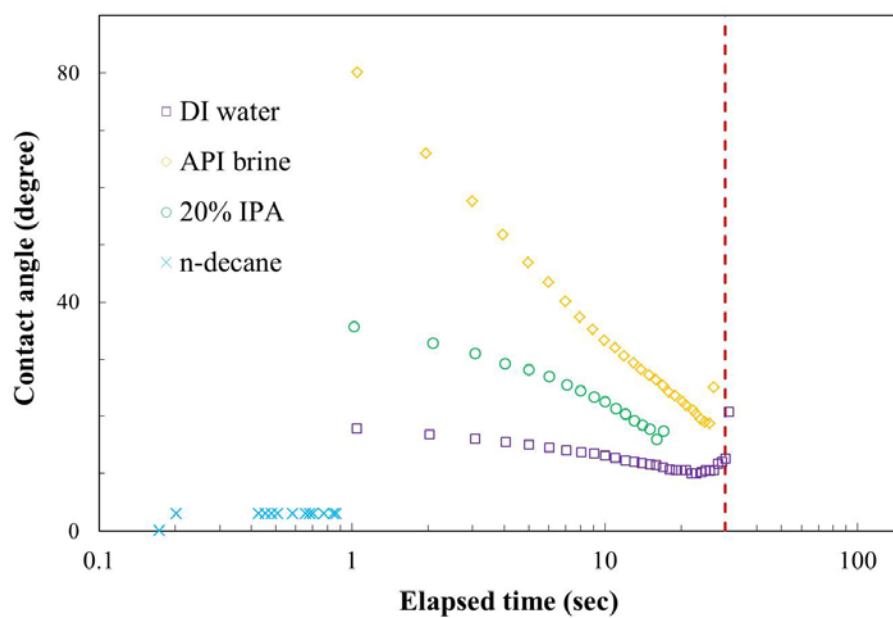
Paddock 5931 D



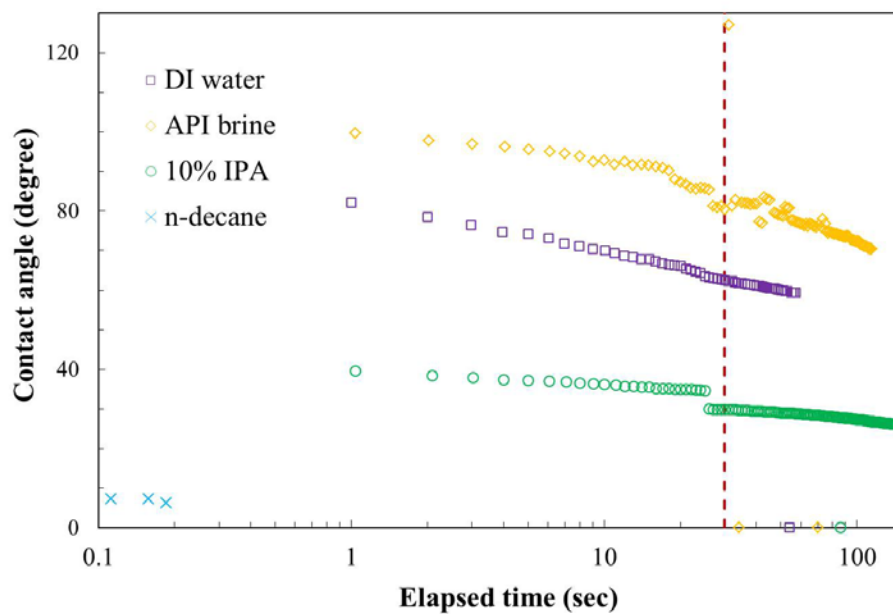
Blinebry 6823 D



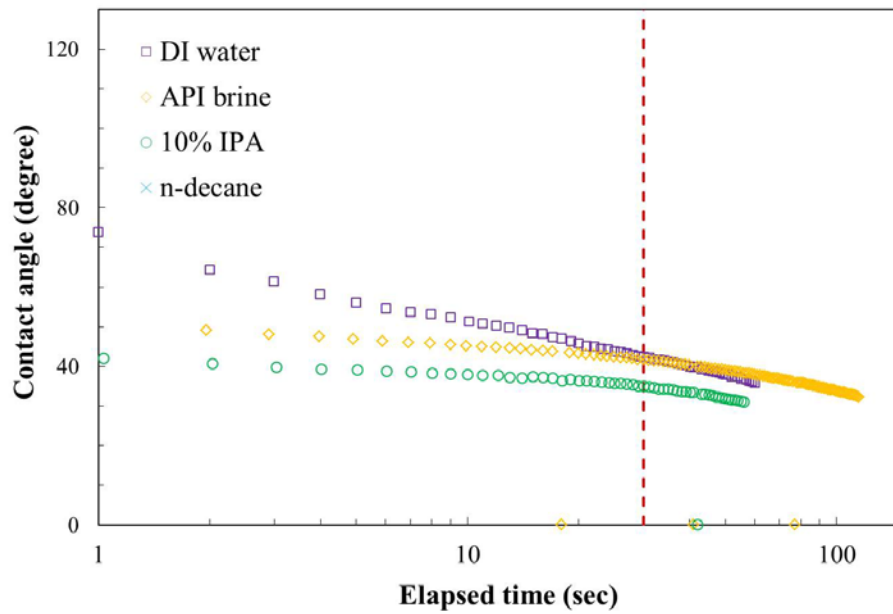
Abo 8952 D



Abo 8956 D



Cisco 11061 LS



Cisco 11097 SS

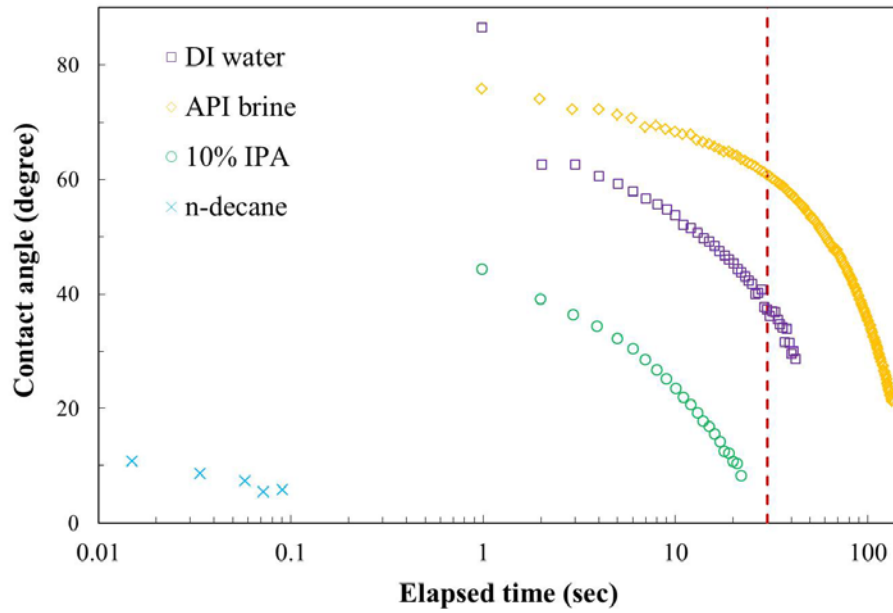


Figure 4-1 Contact angle graphical results.

Pore Connectivity from Fluid Imbibition

Fluid imbibition tests using DI water were run on all the samples in an effort to understand the pore connectivity for each sample and the formation being studied. The amount of fluid uptake over the time interval was measured and recorded on a logarithmic scale with slopes being created to calculate the trend of the data. For most of imbibition runs utilizing DI water as the fluid, 3 slopes (for Stages I, II, and III) were observed with the exception of the shallower samples (Paddock 5931 D and Blinebry 6823 D), which only saw 2 observed slopes (Stages I, and II). The first slope (Stage I, which lasts up to 1 min) can be connected to the initial settling of the sample when first coming in to contact with the fluid. The second slope (Stage II; up to about 1 hr) is attributed to the fluid migration across well connected pores throughout the sample. The third slope, which lasts throughout the remainder of the experiment, generally begins anywhere from the 30 minute mark to about the 90 minute mark. Lower imbibition slopes correlate to poorly connected pore networks. Table 4-2 shows the calculated slopes for all the DI water imbibition runs for each sample, with the average Stage III slope shown in the far right column. The results for each of the 24 hour experiments with log time in minutes on the x-axis and log cumulative imbibition in mm on the y-axis is shown in Figures 4-2, 4-3 and 4-4.

Table 4-2 DI water imbibition slopes with the final slope average

Sample ID	DI Water									Average Slope & Water Saturation			
	6 hr			12 hr			24 hr						
	Slope 1	Slope 2	Slope 3	Slope 1	Slope 2	Slope 3	Slope 1	Slope 2	Slope 3	Slope 2	Slope 2 Water Saturation (%)	Slope 3	Slope 2 Water Saturation (%)
Paddock 5931 D	1.382	0.398	X	X	X	X	1.045	0.459	X	0.429	51.1 %	X	X
Blinebry 6823 D	2.506	0.392	X	1.811	0.473	X	6.347	0.426	X	0.430	84.2 %	X	X
Abo 8952 D	2.267	0.616	0.028	1.136	0.497	0.077	2.117	0.687	0.091	0.600	41.0 %	0.065	53.5 %
Abo 8956 D	1.314	0.616	0.271	2.546	0.469	0.074	0.944	0.518	0.143	0.534	41.4 %	0.163	72.9 %
Cisco 11061 LS	1.142	0.572	0.049	X	X	X	2.04	0.414	0.119	0.493	45.3 %	0.084	64.4 %
Cisco 11097 SS	2.158	0.431	0.072	X	X	X	1.935	0.423	0.139	0.427	71.1 %	0.106	~100 %

The imbibition results of DI water into Yeso (Paddock and Blinebry Members) are shown in Figure 4-2. These two samples are the only ones that did not exhibit a slope 3, but had an average slope for slope 2 right around 0.430 for both samples which is comparable to the slope 2 averages seen in the other 4 samples. The DI water imbibition results for the Abo samples can be seen in Figure 4-3. Both of these samples saw all three slopes with an average ranging from 0.065 in the Abo 8952 D sample to 0.163 in the Abo 8956 D sample. The Cisco DI water imbibition results are seen in Figure 4-4. The average for slope 3 came out to be 0.084 for Cisco 11061 LS and 0.106 for Cisco 11097 SS. The highest slope 2 values was seen in the two Abo samples, which correlates to the fluid passing through the well connected pores until it reaches the top of the sample. Slope 2 correlates to the overall pore connectivity of the sample with higher slopes indicating a well-connected pore network. All of the samples tested in this study had a relatively high slope 2.

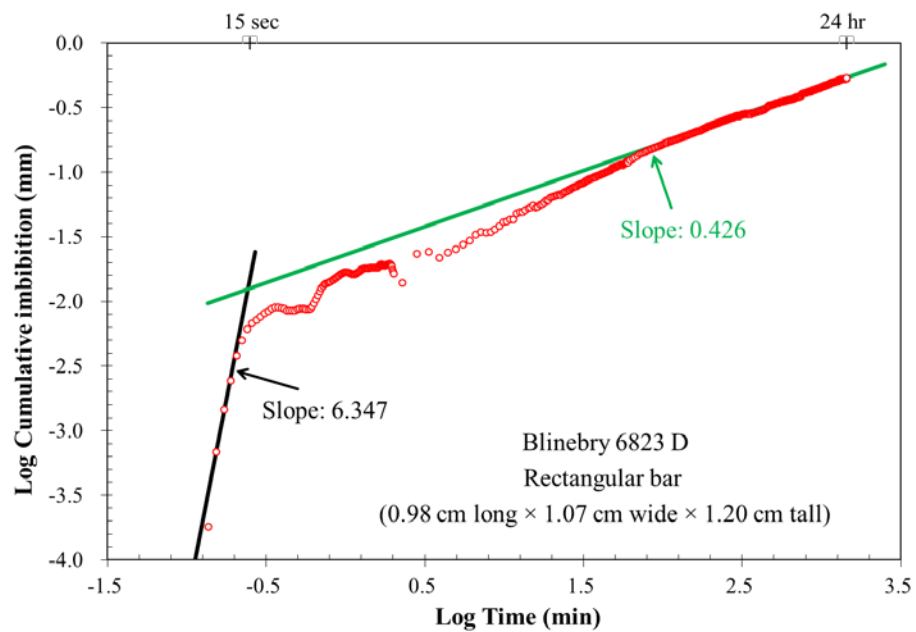
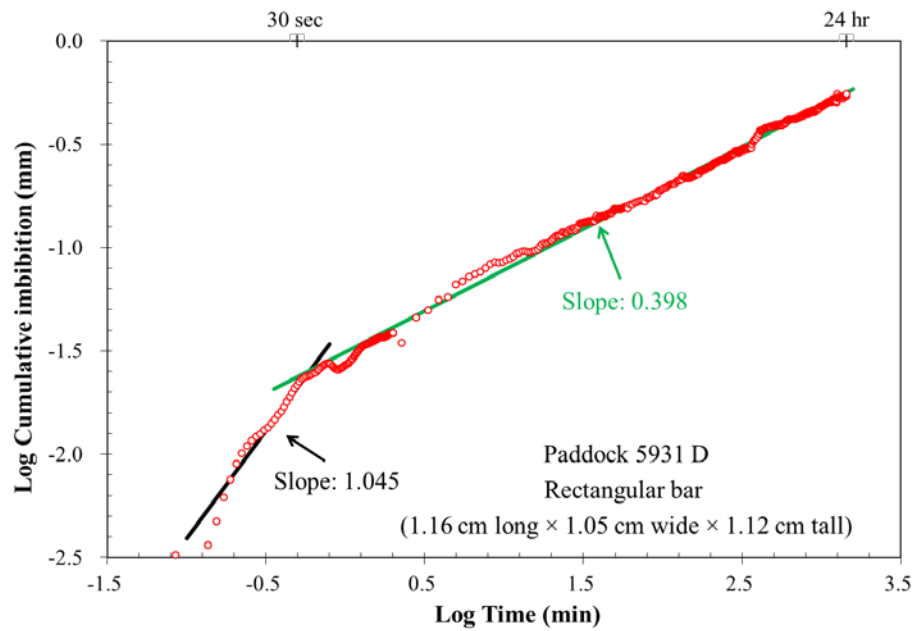


Figure 4-2 Yeso DI water imbibition results.

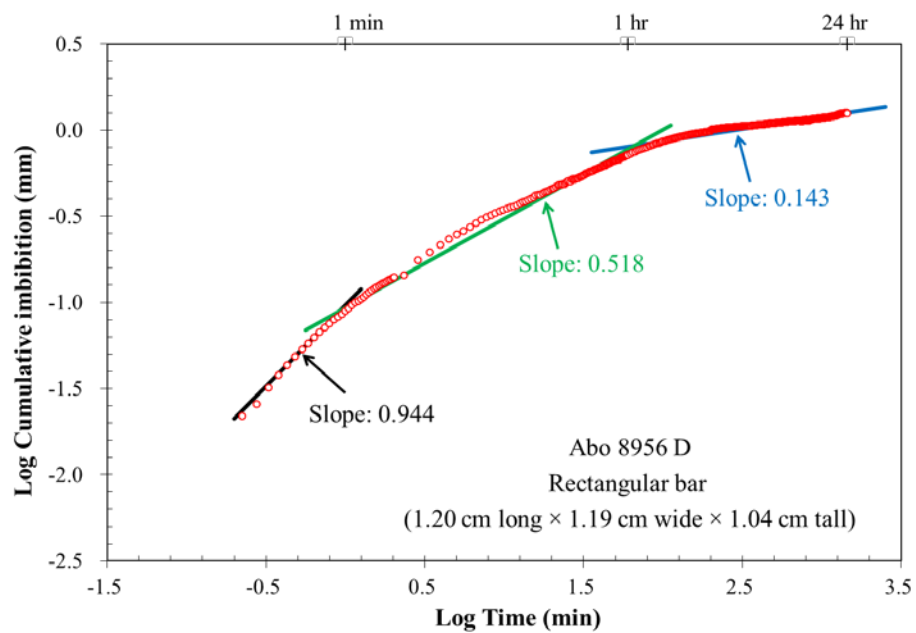
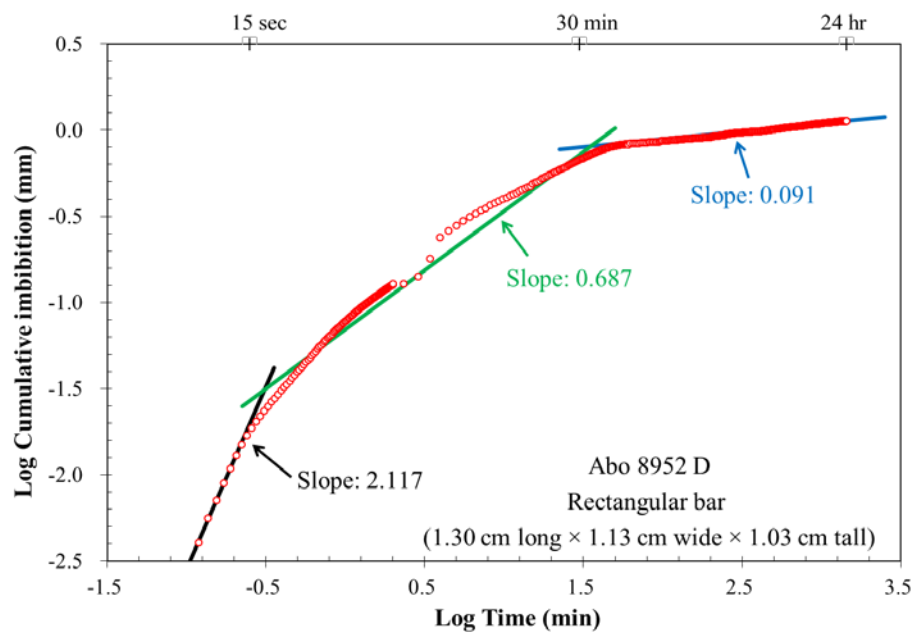


Figure 4-3 Abo DI water imbibition results.

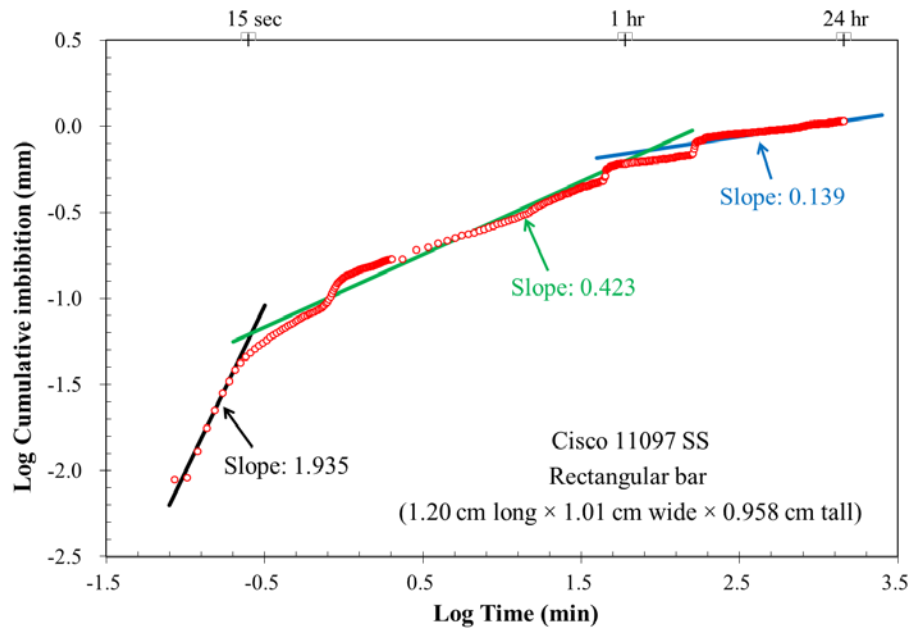
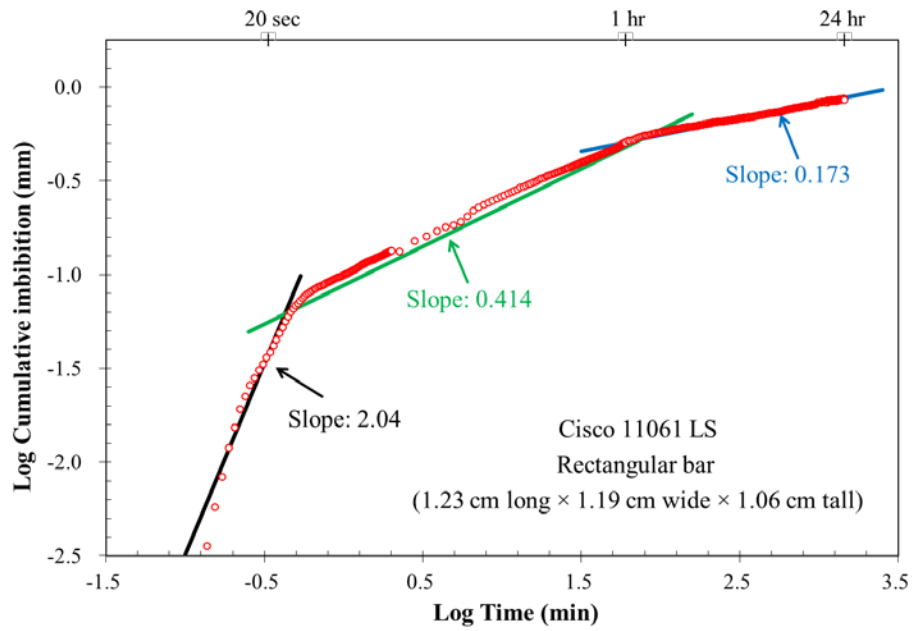


Figure 4-4 Cisco DI water imbibition results.

Fluid imbibition runs with n-decane were attempted on all of the samples but the tests were inconclusive as the samples seemed to lose weight throughout the experiment. When checking the before and after weights of the sample and the holder, it seems that this could be attributed to the holder losing weight throughout the duration of the experiment. All of the n-decane runs lasted for 8 hours and when observing each sample at the duration of the experiment, fluid was noted to have reached the sample top. This observation leads us to believe that the fluid was passing through the pore networks, as to be expected but the offset of the weight loss of the holder was causing the results to be inaccurate.

Pore Connectivity from Vapor Adsorption

Vapor adsorption tests were run on all 6 of the sample utilizing DI water. The process is similar to the fluid imbibition test, only the experiment length is different and the sample is hung a few centimeters above the fluid instead of coming in-to direct contact with the fluid. Each test lasted 3 days with two slopes (Stages I and II) being observed for all samples except the Blinebry 6823 D sample which only had one observed slope (Stage II). Table 4-3 shows the slope values for each sample utilizing DI water as the fluid for vapor adsorption tests. Figure 4-5 shows the vapor adsorption results for the Yeso samples. Slope 1 and 2 for the Paddock 5931 D look similar to those seen in the Abo and Cisco samples as does the slope 2 for the Blinebry 6823 D sample. Figure 4-6 shows the vapor adsorption results for the two Abo samples and Figure 4-7 shows the results for the Cisco samples. All of the observed slopes for slope 2 look comparable except for a relatively low slope of 0.377 for the Cisco 11097 SS sample. The highest recorded slope 2 is seen in the Abo 8956 D sample.

Table 4-3 Vapor adsorption results utilizing DI water as the fluid

Sample ID	DI Water			
	Slope 1	Water Saturation (%)	Slope 2	Water Saturation (%)
Paddock 5931 D	1.350	3.14 %	0.553	55.2 %
Blinebry 6823 D	X	X	0.489	81.5 %
Abo 8952 D	0.900	1.84 %	0.527	24.6 %
Abo 8956 D	1.214	2.09 %	0.616	49.0 %
Cisco 11061 LS	1.988	1.18 %	0.605	88.0 %
Cisco 11097 SS	1.286	1.28 %	0.377	47.7 %

- Stage I (up to about 1 hr)
- Stage II slope (to 72 hr, exp Duration)

During the imbibition, the fluid is taken up by capillary pressure. For vapor adsorption tests, the rock takes up fluid by vapor transport and capillary condensation. Both imbibition and vapor absorption tests consistently show the well-connected pore network of these rocks, from fluid uptake behavior via connected pore network to exhibit slope values close to 1/2.

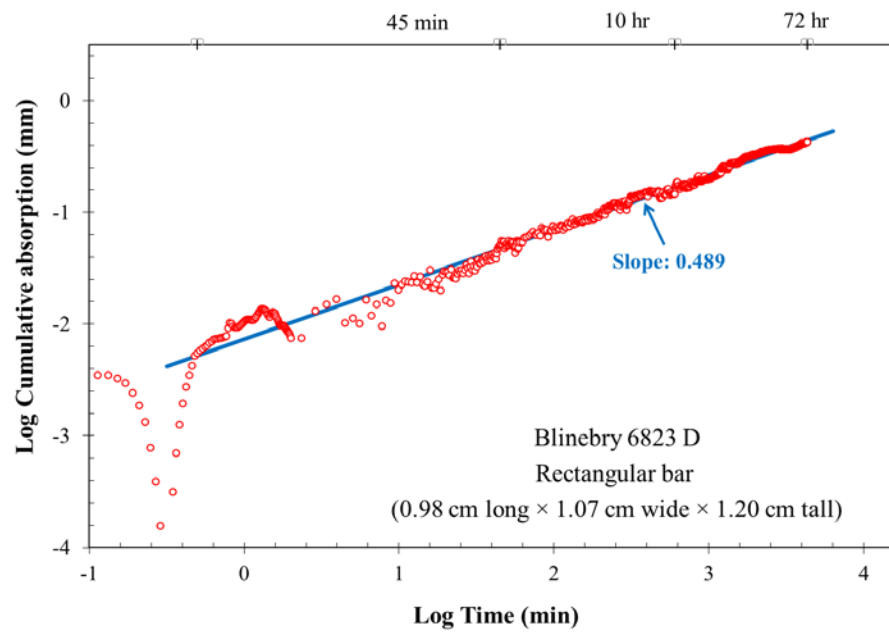
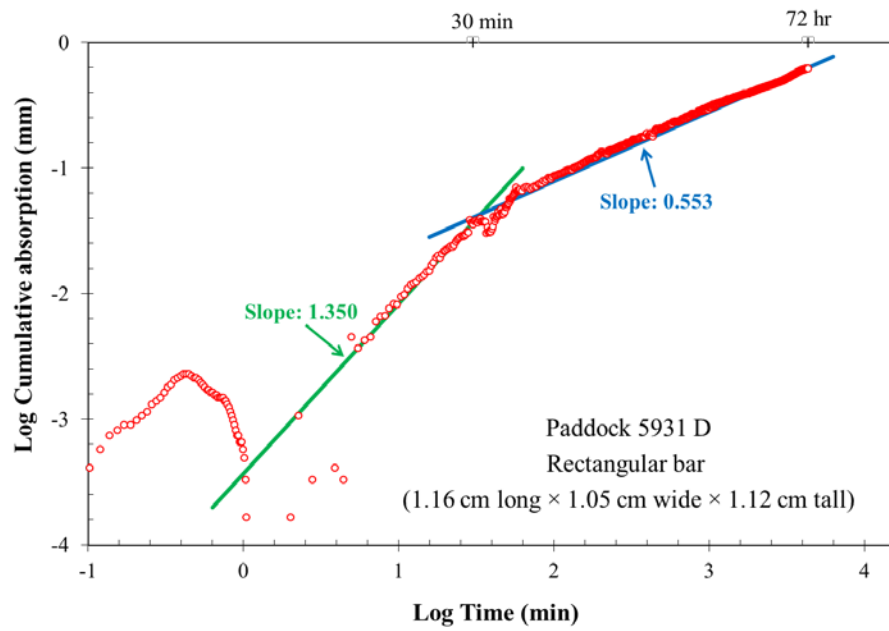


Figure 4-5 Yeso DI water vapor adsorption results.

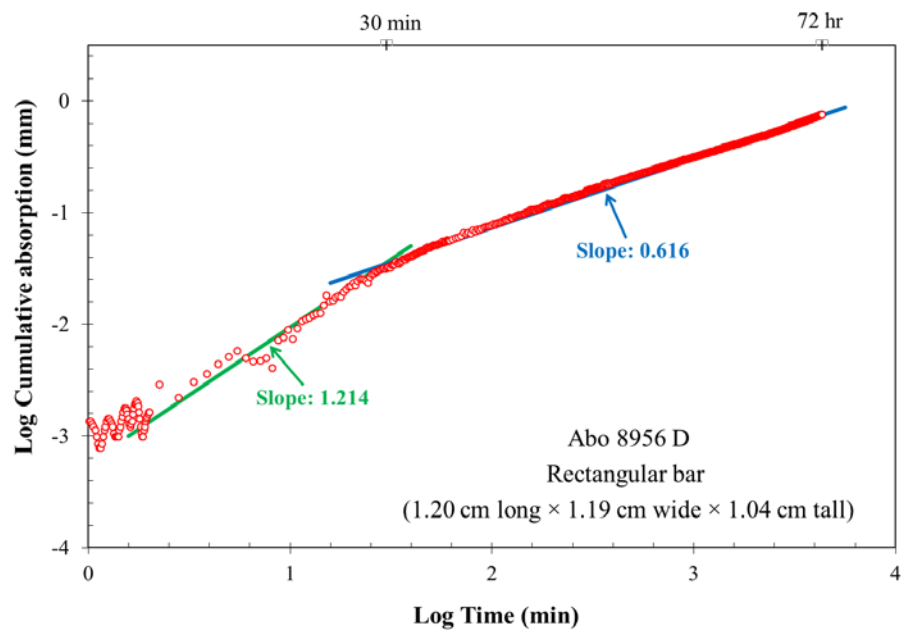
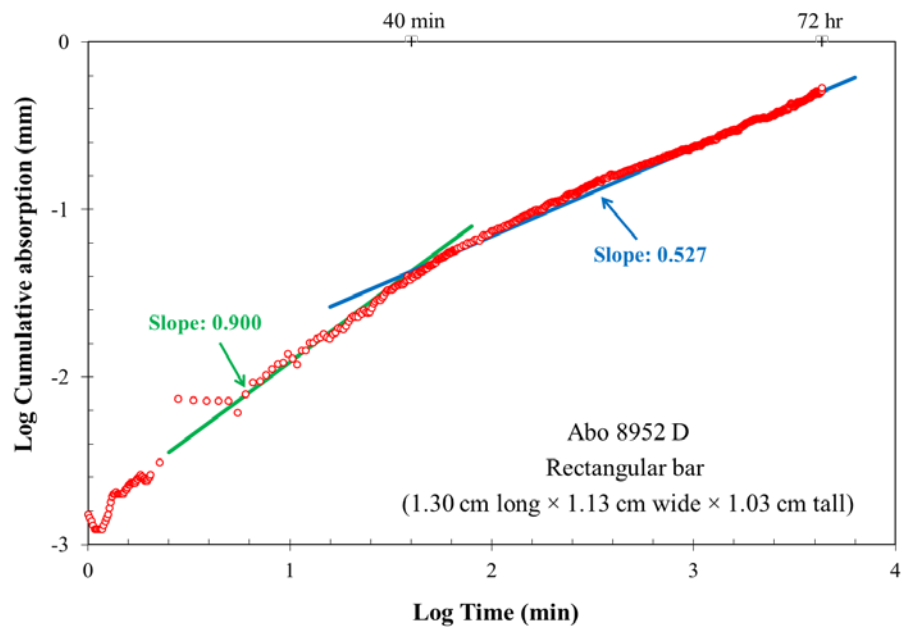


Figure 4-6 Abo DI water vapor adsorption results.

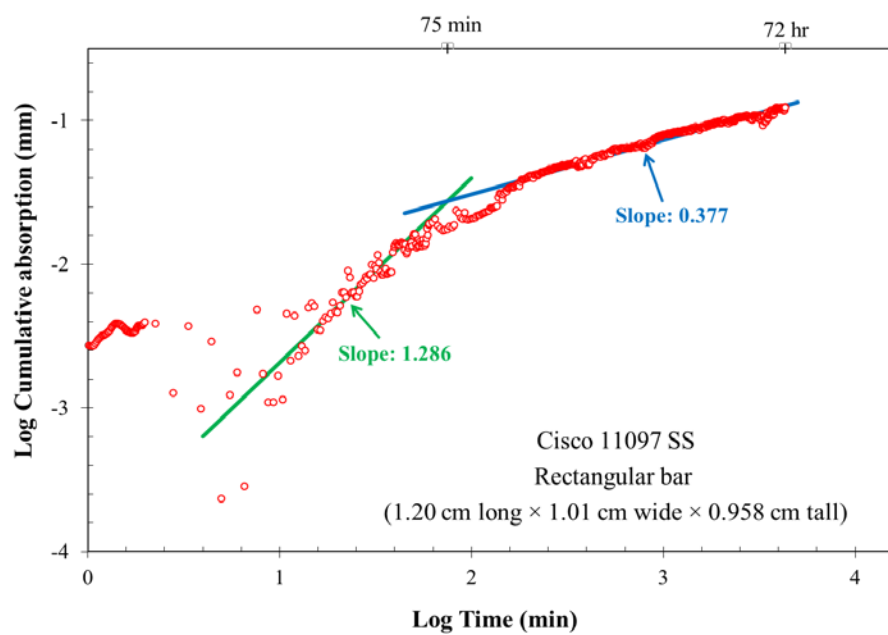
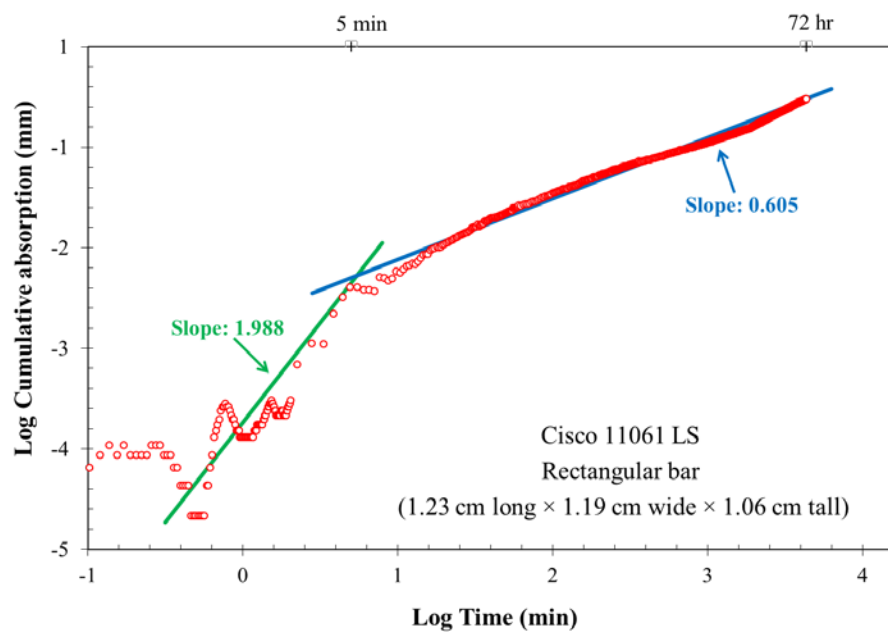


Figure 4-7 Cisco DI water vapor adsorption result

Pore Structure Characteristics from MICP analyses

MICP testing is able to provide a variety of data that can be used to obtain a multitude of petrophysical properties for each sample. Following the methods, which were outlined by Hu (2014), bulk density, porosity, pore-throat size distribution, permeability, tortuosity and other values are able to be quantified and used to characterize pore structure. The results of the MICP analyses are shown in Table 4-4.

Bulk density values ranged from 2.23 g/cm³ the Abo 8952 D sample to 2.77 g/cm³ in the Paddock 5931 D sample. Porosity percentages fell within the normal range seen for all of these formations with the Blinberry 6823 D sample exhibiting the least porosity at 4.1% and the Abo 8952 D sample having the highest porosity at 17.9%. The Abo samples seemed to display the highest porosity values of any of the formations studied.

Inflection points are seen in all of my samples, which represent the increased intrusion of mercury into the pore throats when the capillary pressure has been exceeded. An example of the inflection points can be seen in Figure 4-8, with the intrusion pressure shown on the x-axis and the log differential intrusion shown on the y-axis. These inflection points are used with the modified Washburn equation to come up with the pore-throat size distribution for each sample. In addition, the permeability and tortuosity values are taken from the main inflection point, which in Figure 4-8 is represented by the third arrow from the left. Permeability values ranged from 0.05 mD in the Cisco 11061 LS sample to greater than 39 mD in the Paddock 5931 D sample. Tortuosity values, which are dimensionless, of the main inflection point ranged from 15.4 in the Cisco 11097 SS sample to 291.82 in the Cisco 11061 LS sample, which appeared to be an outlier as the second highest recorded value was 68.19.

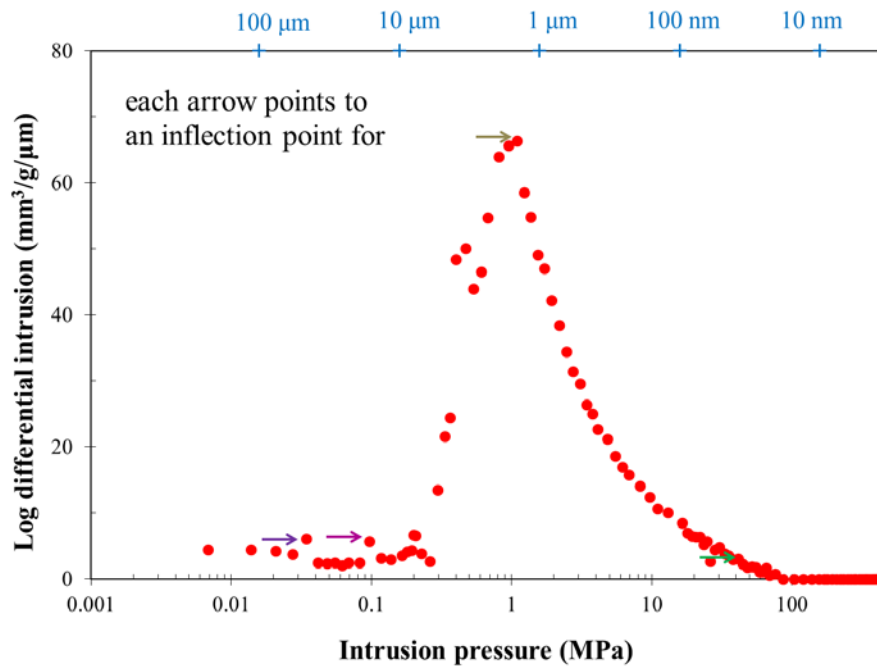


Figure 4-8 Abo 8956 D MICP example of inflection points

Most of the samples studied displayed an average pore size in the range of 1-10 μm , with the exception of the Cisco 11061 LS sample, which had an average pore-throat size within the 0.1-1 μm range and the Paddock 5931 D sample, which fell in the 10-1000 μm range (Fig 4-8, Table 4-5). The Cisco samples contained the highest percent of larger pores with ~ 25% of them falling in the 10-465 μm range along with the one Paddock sample. The pore size distribution can help us classify the percent of micro-, meso- and macro-pores within each sample. The ranges for each of these pore sizes for carbonate rocks are listed below (Tonietto et al., 2014).

- Micropores: < 50 μm
- Mesopores: 50 – 100 μm
- Macropores: > 100 μm

When comparing the data in Figure 4-9 and Table 4-5 with these pore types, it is apparent that the majority of the pores present within the samples of this study fall in the micropore range with the exception of the Paddock 5931 D sample, which has a high percentage of mesopores and macropores.

The Paddock 5931 D sample was the only one that displayed a fracture, which was represented by a spike in intrusion at an intrusion pressure of 0.535 psia with a corresponding pore-throat size of 460 μm . This fracture had to be accounted for as the data was skewed by that data point. The sample displayed a porosity of 10% when the fracture was included as opposed to 6% when adjusting the data to exclude the spike in intrusion. Other characteristics were affected by the fracture including the pore throat distribution, which exhibited a much higher percentage of meso and macropores in the range of 100 – 1050 μm when the data included the fracture. That percentage dropped when processing the data without the fracture.

Table 4-4 Pore structure results obtained from MICP

Sample ID	Sample mass used (g)	Total pore volume (cm ³ /g)	Total pore area (m ² /g)	Median pore-throat diameter D ₅₀ (Volume) (μm)	Median pore-throat diameter (Area) (μm)	Median pore-throat diameter (4V/A) (μm)	Bulk density (g/cm ³)	Apparent (skeletal) density (g/cm ³)	Porosity (%)	Main Inflection Point k (mD)	Main Inflection Point Tortuosity (Dimensionless)
Paddock 5931 D	2.0765	0.0412	0.228	185	0.0815	0.724	2.49	2.78	6.8	39.1	68.2
Blinebry 6823 D	2.0727	0.0153	0.146	1.91	0.0887	0.418	2.70	2.81	4.1	1.21	23.7
Abo 8952 D	2.2413	0.0802	0.454	1.28	0.4621	0.707	2.23	2.72	17.9	2.12	35.5
Abo 8956 D	2.8487	0.0694	0.641	1.21	0.1372	0.433	2.29	2.73	15.9	1.73	38.1
Cisco 11061 LS	2.4388	0.0207	0.289	0.62	0.0967	0.288	2.45	2.58	5.1	0.05	291
Cisco 11097 SS	2.0828	0.0274	0.056	4.79	0.4672	1.951	2.57	2.76	7.0	10.4	15.4

Table 4-5 Pore-throat size distribution (%) from MICP analyses

Sample ID	Pore-Throat Size (μm)					
	0.01-0.05	0.05-0.1	0.1-1	1-10	10-465	10-1000
Paddock 5931 D	0.687	4.350	20.006	13.862		61.095
Blinebry 6823 D	0.866	4.194	20.559	63.641	10.741	
Abo 8952 D	0.214	0.864	21.310	71.423	6.189	
Abo 8956 D	0.988	2.332	29.595	58.004	9.081	
Cisco 11061 LS	1.196	5.902	48.205	18.474	26.223	
Cisco 11097 SS	0.000	0.287	6.100	68.969	24.644	

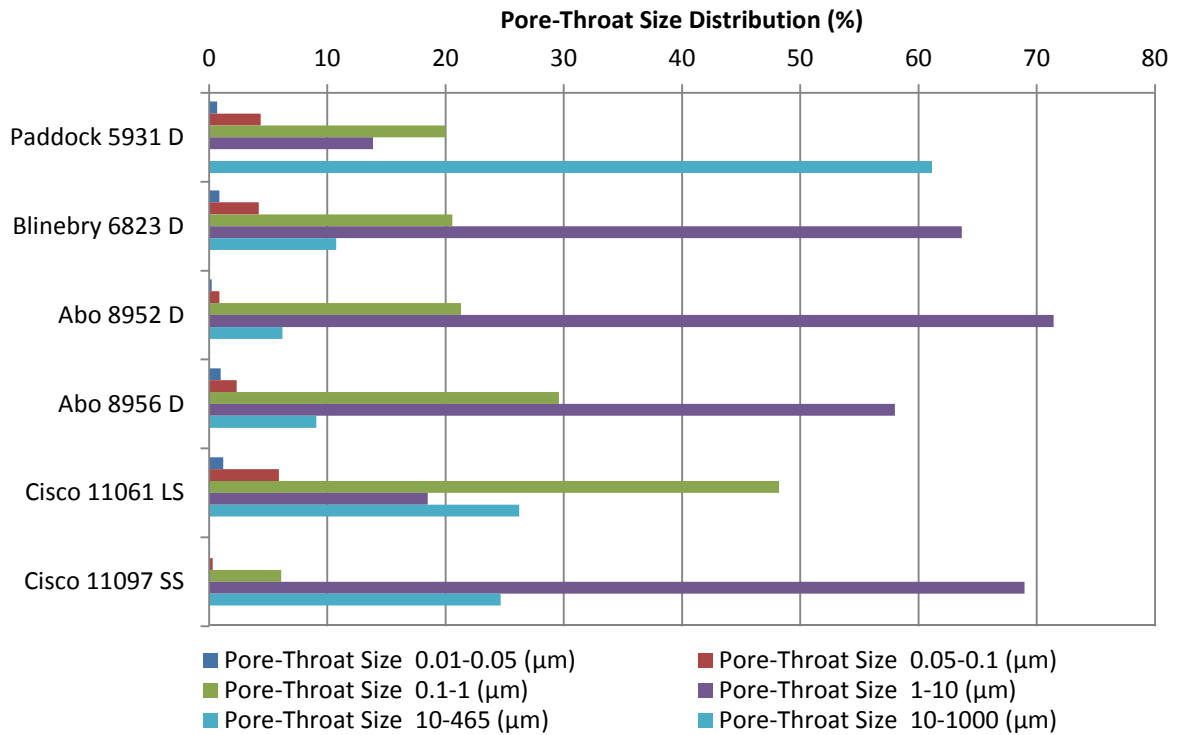
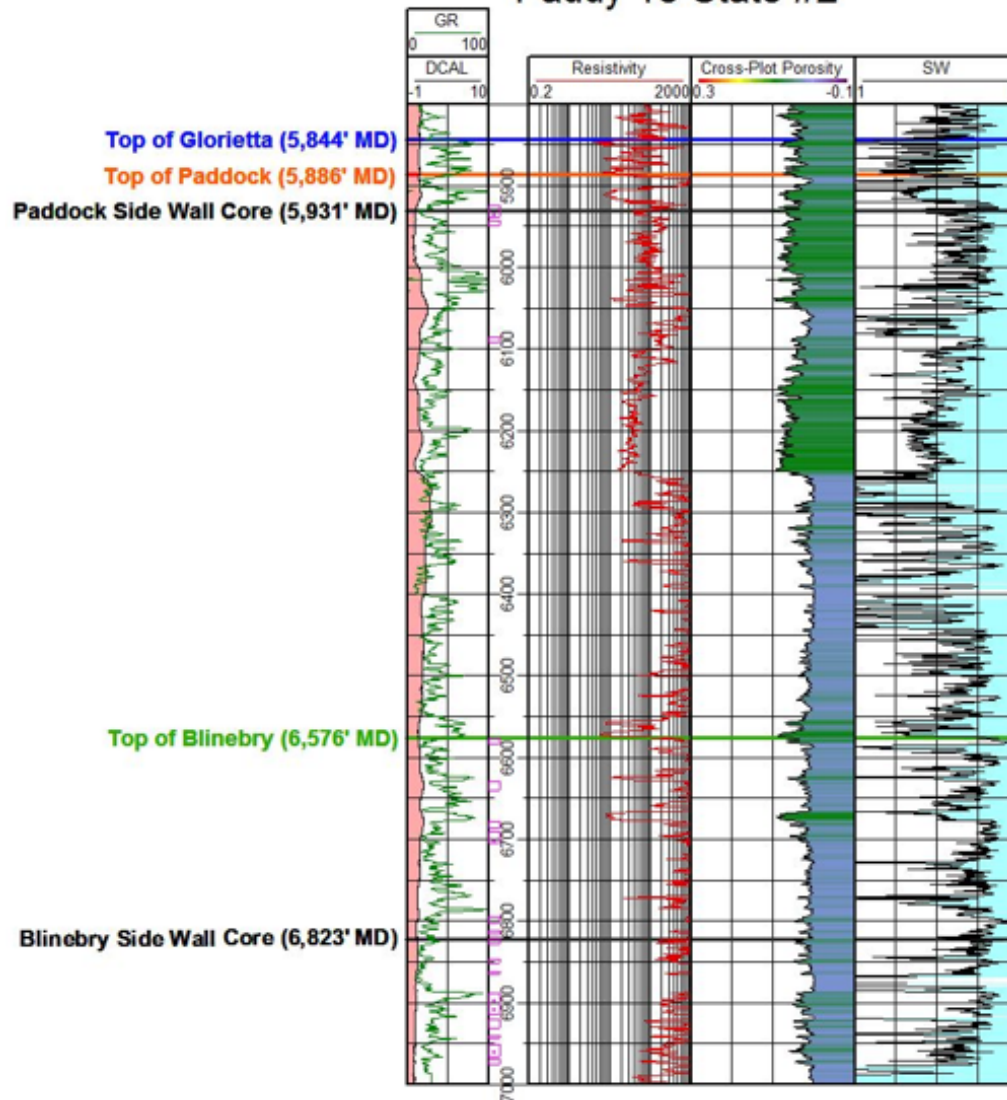


Figure 4-9 Graphical representation of pore size distribution results from MICP

Porosity and Permeability from Log Analyses

Well log analyses were used to provide log derived values for different petrophysical characteristics such as porosity and permeability. These values can be used as a comparison with the core derived data that was previously collected on each of the samples as well as what was performed at the University of Texas at Arlington. The results for water saturation curve for the Paddy 18 State #2 well are shown in Figure 4-10. Also shown in that figure are the true resistivity and cross-plot porosity curves used to generate the water saturation and the log derived values compared with the laboratory derived values for porosity and permeability. Figure 4-11 shows the same results for the Gen Montcalm 25 State #1 well and Figure 4-12 displays the results for the Abenaki 10 State #1 well.

CML Exploration Paddy 18 State #2



Paddock 5931 D

Porosity (%)		Permeability (mD)	
Cross-Plot Porosity (Log)	10.5	Log Derived Permeability	~ 4.5
Boyle's Law Porosimeter	10.1	Hassler Sleeve Permeameter	3.58
MICP	6.8 10.3	MICP	39.1

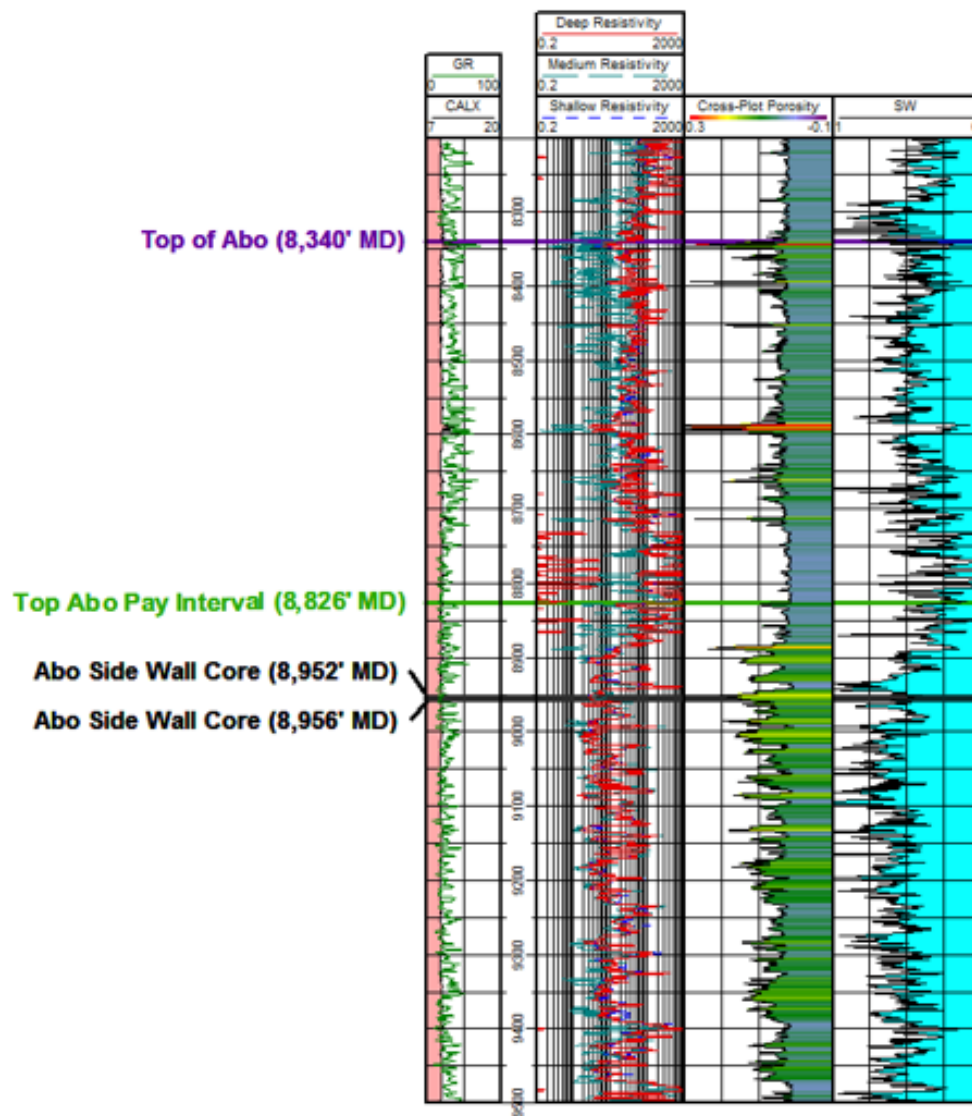
Red – denotes porosity value including data spike

Blinebry 6823 D

Porosity (%)		Permeability (mD)	
Cross-Plot Porosity (Log)	5.0	Log Derived Permeability	~ 0.7
Boyle's Law Porosimeter	5.3	Hassler Sleeve Permeameter	0.26
MICP	4.1	MICP	1.21

Figure 4-10 Log analyses of Paddy 18 State #2 well with porosity and permeability comparisons (created in Petra).

ConocoPhillips
Gen Montcalm 25 State #1



Abo 8952 D

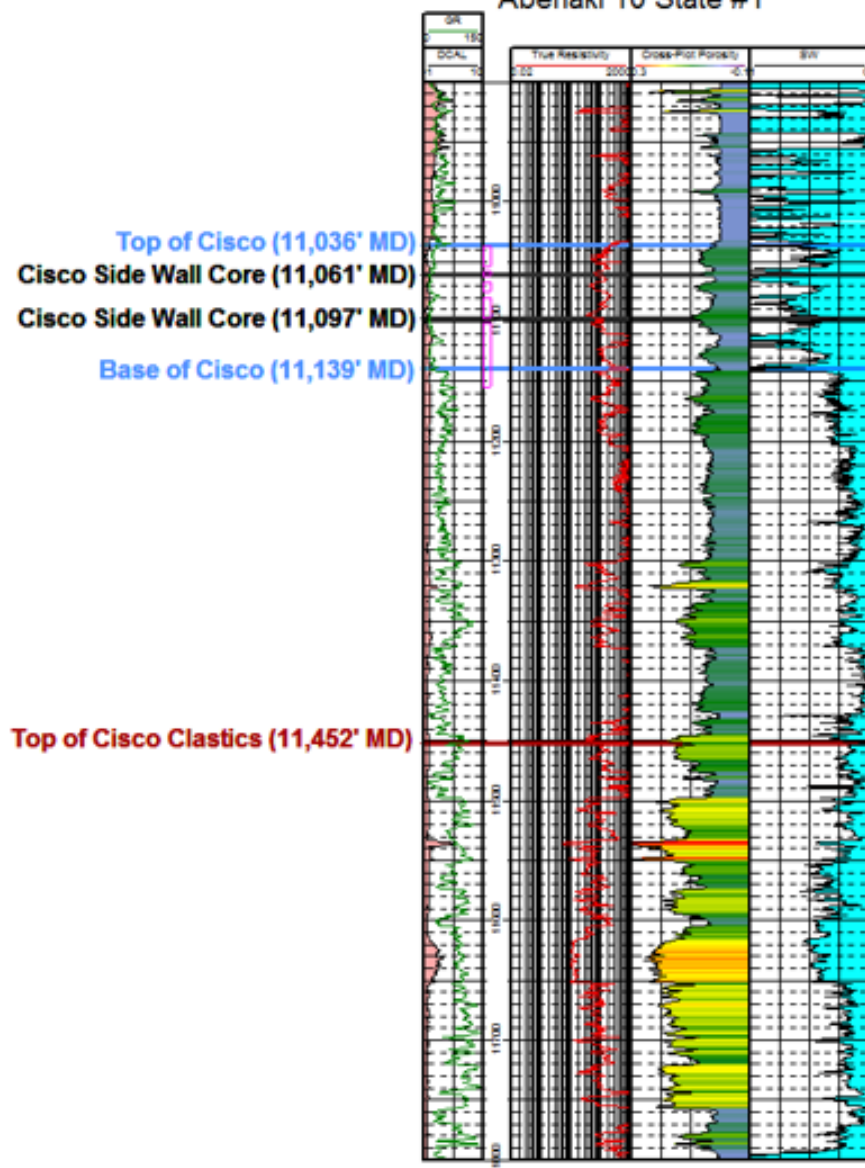
Porosity (%)		Permeability (mD)	
Cross-Plot Porosity (Log)	17.9	Log Derived Permeability	~ 7.0
Boyle's Law Porosimeter	20.9	Hassler Sleeve Permeameter	4.11
MICP	17.9	MICP	2.12

Abo 8956 D

Porosity (%)		Permeability (mD)	
Cross-Plot Porosity (Log)	14.8	Log Derived Permeability	~ 2.8
Boyle's Law Porosimeter	14.7	Hassler Sleeve Permeameter	0.91
MICP	15.9	MICP	1.73

Figure 4-11 Log analyses of Gen Montcalm 25 State #1 well with porosity and permeability comparisons (created in Petra)

CML Exploration
Abenaki 10 State #1



Cisco 11061 LS

Porosity (%)		Permeability (mD)	
Cross-Plot Porosity (Log)	7.0	Log Derived Permeability	~ 0.25
Boyle's Law Porosimeter	10.2	Hassler Sleeve Permeameter	0.43
MICP	5.1	MICP	0.05

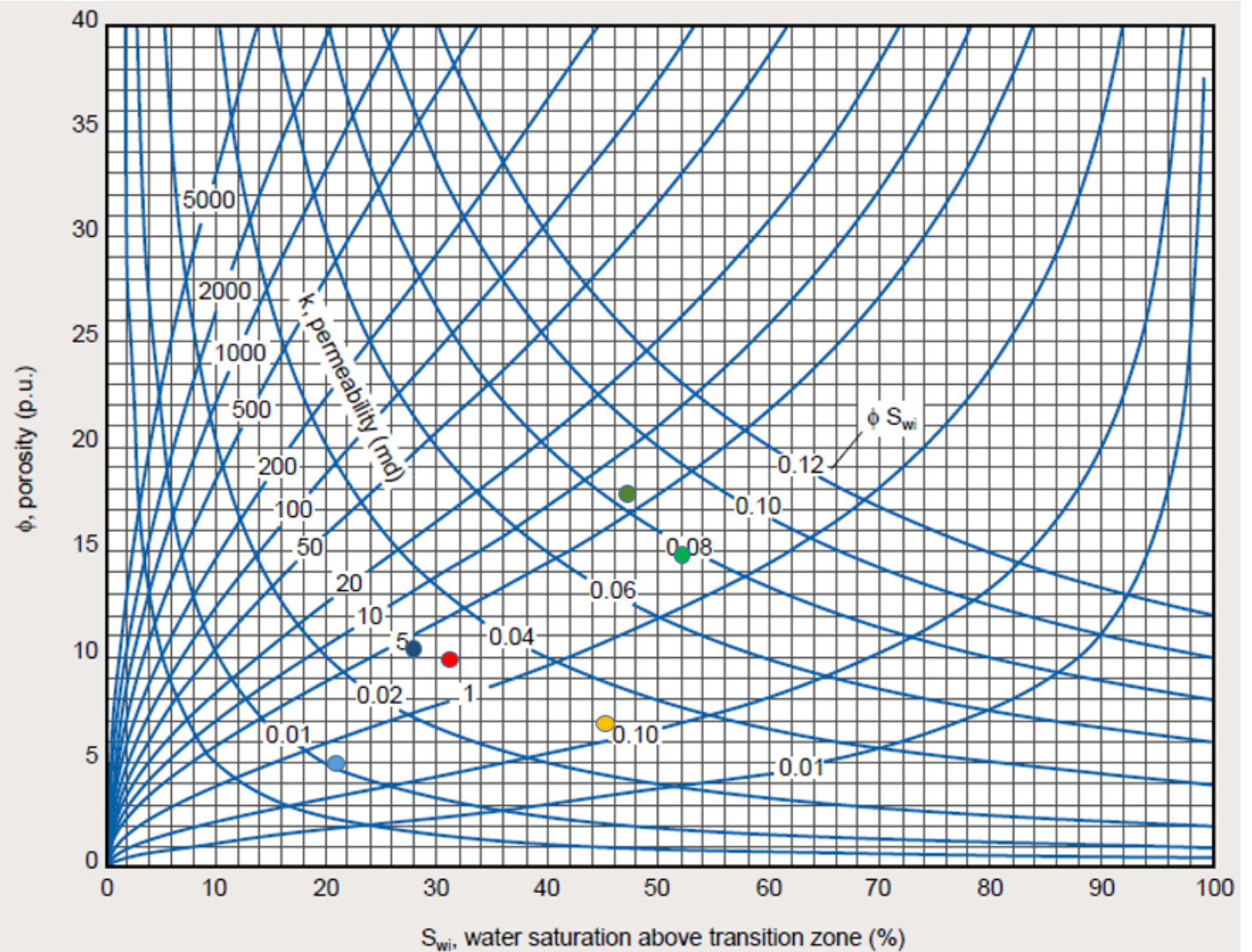
Cisco 11097 SS

Porosity (%)		Permeability (mD)	
Cross-Plot Porosity (Log)	9.9	Log Derived Permeability	~ 3.2
Boyle's Law Porosimeter	8.5	Hassler Sleeve Permeameter	1.69
MICP	7.0	MICP	10.4

Figure 4-12 Log analyses of Abenaki 10 State #1 well with porosity and permeability comparisons (created in Petra)

Log-derived permeability was created using the Schlumberger tornado chart with water saturation on the x-axis and porosity on the y-axis. The results for the permeability based off of the log-derived porosity and water saturation values can be seen in Figure 4-13. When comparing the log-derived permeability with the permeability values collected from MICP and Hassler sleeve permeameter with nitrogen under 300 psi confining pressure in Weatherford Laboratories, the results are comparable (Figures 4-10, 11, 12). Porosity values taken from the logs varied by a few percentage points for a couple of samples, but seemed to be comparable to what was measured from the sidewall cores. This variation may be due to the log taking an average reading further into the rock in comparison to measuring on the centimeter scale within the laboratory. It's reported that the influence volume of well logging can vary from around 25-50 cm for neutron, density and gamma ray logs to more than 150 cm for resistivity logs (Mazaheri et al., 2015).

	Sample ID	Porosity	Sw	Permeability
●	Paddock 5931 D	10.5%	27.5%	~ 4.5 mD
●	Blinberry 6823 D	5.0%	20.8%	~ 0.7 mD
●	Abo 8952 D	17.9%	47.0%	~ 7.0 mD
●	Abo 8956 D	14.8%	52.1%	~ 2.8 mD
●	Cisco 11061 LS	7.0%	45.6%	~ 0.25 mD
●	Cisco 11097 SS	9.9%	31.1%	~ 3.2 mD



© Schlumberger

Figure 4-13 Tornado chart showing the log derived permeability values for each sample (Schlumberger, 2009)

Chapter 5

Discussion and Conclusion

Wettability

All of the contact angle measurement tests resulted in the samples exhibiting an oil-wetting behavior. This observed hydrophobic affinity towards n-decane describes the tendency for each sample to attract oil over water. However, this does not describe what the rock may be saturated with at reservoir depth. In the presence of oil, these reservoirs will prefer this fluid over water but the overall water saturation, which was determined through log analyses, will give us insight into what type of fluid is occupying the pores at certain depths. The variations between the four fluids (DI water, API Brine, 10% or 20% IPA and n-decane) shows us how each sample can react differently between the different fluids. For example, the Cisco 11097 SS sample had a lower contact angle for 10% IPA than the rest of the samples tested. This may be due to a different mineral composition as this sample was described to be more of a sandstone.

Pore Connectivity

As seen in the results, the different slopes from both fluid and vapor adsorption relate to different types of pore networks and can indicate the pore connectivity of each sample. The Abo samples display the highest values for slope 2, which correlates to the well-connected pore networks. The Yeso (Paddock and Blinbry) samples and the Cisco samples had slightly lower slope 2 values in comparison to the Abo samples but still exhibited fairly high slopes, which indicates they all had a good amount of well-connected pore throats. On almost all of the runs including the 6 hour tests, the fluid was observed on the top of the samples to indicate both DI water and n-decane move through the sample, via the well-connected pore networks at a relatively fast rate (e.g., to travel 1 cm within 1 hr for the imbibition tests). The sudden jumps in cumulative imbibition that is

seen in some of the samples (e.g., in the Cisco 11097 SS sample) may be attributed to micro-fractures within the samples as the fluid moves quicker through these volumes.

Pore Structure Characteristics from MICP Analyses

The data collected from MICP provides us with a wide variety of data. The formation with the highest recorded porosity values was the Abo, which had porosity values greater than 15%. This is also displayed from the total pore volume and total pore area as these values increase with higher porosity percentages for each sample. Permeability values varied as the Yeso Formation (Paddock and Blinbry Members) recorded the highest readings from 16 – 39 mD. The lowest value was seen in the Cisco 11061 LS sample as it displayed a permeability of 0.05 mD. Fluid flow through this sample (Cisco 11061 LS) was found to be most difficult in comparison to the other samples studied as it also yielded the highest tortuosity value at 291.8.

Fluid flow within the Cisco 11061 LS sample as well as the rest of the samples may also be related to the pore-throat size distribution that was determined through MICP. For most of the samples, the majority of the pore-throat sizes fell within the 1-10 μm range and produced values for permeability between 1 – 16 mD. The Paddock 5931 D sample however had the highest percentage of larger pore-throats with 61% of its pore-throat sizes being greater than 10 μm . This sample also had the highest permeability as previously mentioned. The same correlation can be made for the Cisco 11061 LS sample that had the lowest permeability as the majority of its pore-throat sizes were smaller, falling in the 0.1-1 μm range.

Comparisons of Porosity and Permeability from Multiple Approaches

The log analyses displays values for porosity, resistivity and water saturation over a larger interval in comparison to the lab-derived values taken from side wall cores at specific depths. Logs measure further into the rock and take an average over that

interval, which allows for a more general correlation to be made. The water saturation curve created using Archie's equation and the method outlined in the methods section, gives us an idea of what fluid may be occupying the pores at the displayed depths. This is important when deciding where we may want to perforate a well as it highlights the zones that may be more water wet. This is seen in where the Paddy 18 State #2 well was perforated within the Blinebry (figure 5-1), with the perforations marked in purple and yellow arrows pointing to the corresponding water saturations.

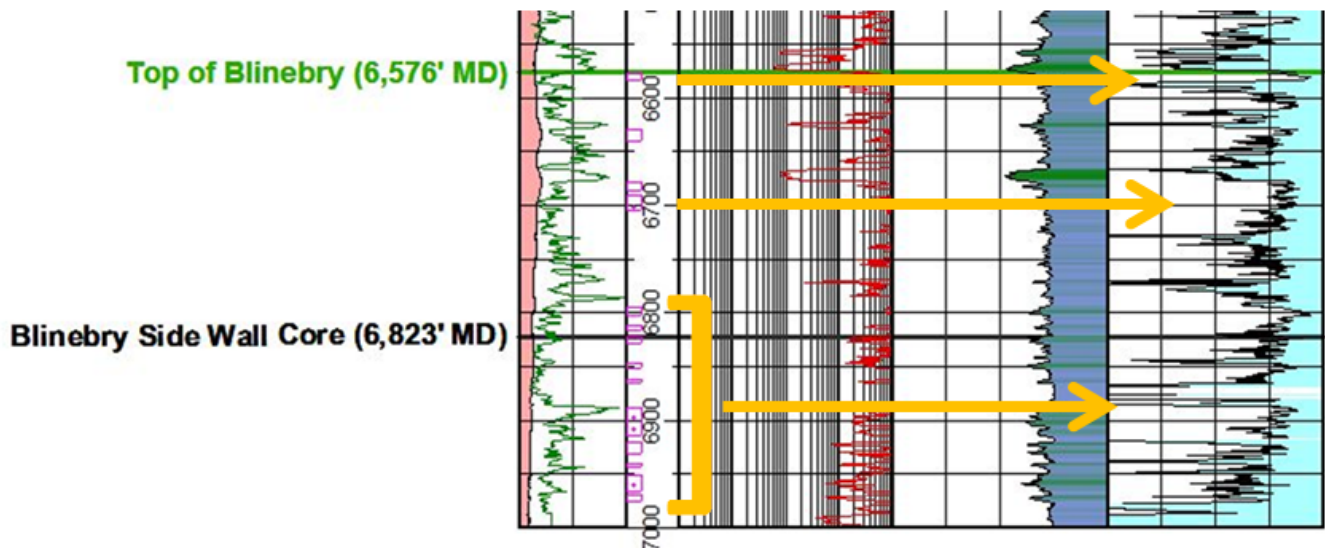


Figure 5-1 Paddy 18 State #2 perforations compared to Sw

Cross-plot porosity values were within a couple percentage points of the laboratory derived values obtained through MICP at UTA and the Boyle's Law Porosimeter with helium at a commercial laboratory (Weatherford Laboratories, Rotary Laboratories), with the exception of the MICP value for the Paddock 5931 D.. The MICP porosity of the Paddock sample with the fracture included came out to be 10.2%, which would have fallen within a 0.5% of the other derived values. This makes sense as the

log-derived values would have included these fractures when taking measurements in the bore hole.

As shown in the Results section, the cross-plot porosity was plotted against the water saturation values for each sample depth to produce a log derived permeability value. These values were comparable to the laboratory-derived values that were performed through MICP at UTA and in commercial laboratories using the Hassler sleeve permeameater method. In comparison the log derived method utilizing the Schlumberger tornado chart followed the same trends of the values obtained using the other methods and in a lot of cases were within the same order of magnitude of the other values. Having these log calculations derived over the whole formation can provide a general correlation of permeability over a larger depth range.

All of the values obtained in this study seem reasonable with the exception of a few of the permeability values. Between the three methods, the permeability values obtained through the Hassler Sleeve Permeameater utilizing nitrogen at a confining pressure of 300 psi seem to be the most accurate as this experiment is designed specifically to obtain permeability values. Log derived values seem reasonable and give good trends for permeability, but some assumptions had to be made when calculating, which might lead to not as precise measurements.

The porosity measurements seemed to compare well between the three methods used to obtain the values. The values that appear to be the most accurate would belong to the laboratory methods (MICP and Boyle's Law Porosimeter) as they take direct measurements from the experimental runs. The log derived porosity matched up well with the laboratory derived values but only gives an inferred value, which ends up not being as accurate. This method is good however in providing a reasonable value over the entire log section being studied.

Conclusion

Petrophysical data was collected for each formation through the use of contact angle measurements, spontaneous imbibition and vapor adsorption tests, mercury injection capillary pressure (MICP), and log analyses. Contact angle measurements utilizing DI water, API brine, 10% or 20% IPA and n-decane were performed to determine whether the samples were oil-, water- or mixed-wet. All of our samples are preferentially oil-wetting with slight variations between each of the samples.

Imbibition tests were run using DI water and n-decane. For the DI water test runs all of the samples displayed a well-connected pore system with the Abo samples displaying the highest connectivity according to the slope 2 value. The n-decane runs although unsuccessful when recording data, did show fluid on the sample top, proving that the fluid was successfully moving through the sample. Similar results were seen when using these fluids for vapor adsorption.

MICP analyses provide a variety of pore structure data, which include porosity, pore-throat size distribution, permeability, and tortuosity. The Abo samples display the highest porosities while the Yeso samples display the highest permeability values. The majority of the pore sizes for most of the samples falls within the 1 – 10 μm range with the only exceptions being the Paddock 5931 D sample and the Cisco 11061 LS sample. The Paddock sample, after excluding a fracture, has a high percentage of pores ranging from 10 – 1000 μm . The Cisco 11061 LS sample had a high percentage of smaller pores ranging from 0.1 – 1 μm .

The log analyses performed utilize digital logs to create curves for cross-plot porosity and water saturation, which are used to generate permeability values from a Schlumberger tornado chart. The logs provide petrophysical data over the entire formation being studied and are compared with the lab derived data. Water saturation

values are used to generate permeability as well as give an idea of how much water may be occupying the pores at certain depths. Cross-plot porosity values prove to be very similar as does permeability when comparing them with the core measured values generated through laboratory techniques.

Recommendations

In order to produce these reservoirs more effectively within the Northwest Shelf of New Mexico, more research is needed. For example, mineralogy composition imaging of scanning electron microscopy need to be obtained in an effort to draw comparisons between the data collected in this study. As more wells are drilled and different completion techniques are utilized, such data will become available and well productivity will be effectively improving.

Appendix A

Laboratory methods at Weatherford Laboratories



CORE ANALYSIS PROCEDURES
FOR
CML EXPLORATION, LLC
PADDY '18' STATE # 2
LEA COUNTY, NEW MEXICO

The Rotary Sidewalls were picked up by Weatherford Laboratories.

Gases from the Sidewalls were measured by Hot Wire Chromatography and reported in Gas Units.

A brief Lithological Description of the Sidewalls was recorded.

A description of the Fluorescence of the Sidewalls was recorded.

Ultraviolet Light Photographs were taken of the Sidewalls for a permanent record.

Natural Light Photographs were taken of the Sidewalls for a permanent record.

Composite Photographs of the Sidewall End Trims were taken under Natural and Ultraviolet Light.

The Sidewalls were extracted utilizing the Dean Stark method.

The fluids were measured by the Dean Stark method.

Porosities were measured in a Boyle's Law Porosimeter utilizing Helium.

Permeabilities were measured in a Hassler Sleeve Permeameter utilizing Nitrogen at 300 psi confining pressure.

Test samples of a known permeability were measured before and after the Sidewall permeabilities were measured.

Appendix B

Laboratory methods at Rotary Laboratories



CORE ANALYSIS PROCEDURES

FOR

PATTERSON PETROLEUM LP

GEN MONTCALM 25 STATE # 1

LEA COUNTY, NEW MEXICO

The Rotary Sidewalls were delivered to Rotary Laboratories, Inc.

Gases from the Sidewalls were measured by Hot Wire Chromatography and reported in Gas Units.

A brief Lithological Description of the Sidewalls was recorded.

A description of the Fluorescence of the Sidewalls was recorded.

Ultraviolet Light Photographs were taken of the Sidewalls for a permanent record.

Natural Light Photographs were taken of the Sidewalls for a permanent record.

Composite Photographs of the Sidewall End Trims were taken under Natural and Ultraviolet Light.

The Sidewalls were extracted utilizing the Dean Stark method.

The fluids were measured by the Dean Stark method.

Porosities were measured in a Boyle's Law Porosimeter utilizing Helium.

Permeabilities were measured in a Hassler Sleeve Permeameter utilizing Nitrogen at 300 psi confining pressure.

Test samples of a known permeability were measured before and after the Sidewall permeabilities were measured.

References

- Broadhead, R. F., and S. W. Speer. 1993. Oil and Gas in the New Mexico Part of the Permian Basin. New Mexico Geological Society. pp. 293-300.
- Buckley, S.E., and M.C. Leverett. 1941. *Mechanism of Fluid Displacement in Sands*. More?
- Carleton, A.T. 1977. Vada Pennsylvanian; in A symposium of the oil and gas fields of southeastern New Mexico, 1977 supplement: Roswell Geological Society, pp. 212-213.
- Chukwuma, F. 2015. *Nanopetrophysics of the Utica Shale, Appalachian Basin, Ohio, USA*. M.S. Thesis, the University of Texas at Arlington, USA.
- DrillingInfo, 2017. www.drillinginfo.com
- Doveton, J.H. 1999. *Basics of Oil and Gas Log Analysis*. Kansas Geological Survey: p. 24
- Dutton, S.P., E.M. Kim, R.F. Broadhead, C.L. Breton, W.D. Raatz, S.C. Ruppel, and C. Kerans. 2004. Play Analysis and Digital Portfolio of Major Oil Reservoirs in the Permian Basin: Application and Transfer of Advanced Geological and Engineering Technologies for Incremental Production Opportunities. Bureau of Economic Geology. Available at

http://www.beg.utexas.edu/files/content/beg/research/permianbasin/PA_FinlRpt.pdf. Accessed 10 April 2017.

Encyclopædia Britannica, inc., 02 May 2013. Web. 27 Mar. 2017.
<https://www.britannica.com/place/Permian-Basin>

Galley, J.E. 1955. *Oil and Gas in the Permian Basin of Texas and New Mexico*. Read before the association at New York, March 29, 1955. Published by permission of Shell Oil Company.

Gao, Z.Y. , Q.H. Hu, and H.C. Liang. 2013. *Gas diffusivity in porous media: Determination by mercury intrusion porosimetry and correlation to porosity and permeability*. Journal of Porous Media, 16(7): 607-617

Hager, J., 1998. *Steam Drying of Porous Media*. Ph.D. Thesis, Department of Chemical Engineering, Lund University, Sweden, 155 pp.

Hemmesch, N.T., N.B. Harris, C.A. Mnich, and D. Shelby. 2014. *A sequence-stratigraphic framework for the Upper Devonian Woodford Shale, Permian Basin, west Texas*. AAPG Bulletin, 98(1): 23-47.

Hu, Q., R.P. Ewing, and H.D. Rowe. 2015. *Low Nanopore Connectivity Limits Gas Production in Barnett Formation*. Journal of Geophysical Research: Solid Earth

Katz, A.J., and A.H. Thompson. 1986. *Quantitative Prediction of Permeability in Porous Rock*. The American Physical Society.

Lopez, R., and A. 2007. Soria. *Kinematical description of the spontaneous imbibition processes*. WSEAS International Conference on Fluid Mechanics and Aerodynamics

Loucks, R.. 2008. *Review of the Lower Ordovician Ellenburger Group of the Permian Basin, West Texas*. Bureau of Economic Geology Jackson School of Geosciences. The University of Texas at Austin. p. 1-2

Ma, S., N.R. Morrow, X. Zhou, and Zhang. 1994. *Characterization of Wettability from Spontaneous Imbibition Measurements*. Western Research Institute - University of Wyoming

Masoudi, R., M.H. Halim, H. Karkooti, M. Othman. 2011. *On the Concept and Challenges of Water Saturation Determination and Modeling in Carbonate Reservoirs*. International Petroleum Technology Conference

Mazaheri, A., H. Memarian, B. Tokhmechi, and B.N. Araabi. 2015. *Developing fracture measure as an index of fracture impact on well-logs*. Energy Exploration & Exploitation 33(4): 555-574

Morris, R.L., and W.P. Biggs. 1967. *Using Log-Derived Values of Water Saturation and Porosity*. Shlumberger Well Services

Murchison Oil & Gas, Inc. 2010. *Geographic Footprint*. Released on January 1, 2010.

Available at <http://www.murchisonoil.com/about/permian-basin.html>. Accessed
25 June 2016

Quintero, R.P. 2016. *Coupled Geochemical and Nano-Petrophysical Study of The Spraberry-Wolfcamp Trend West Texas, U.S.A.* M.S. Thesis, Department of Science, University of Texas at Arlington, USA.

Saller, A. 2013. *Sequence Stratigraphy of Classic Carbonate Outcrops in West Texas and Southeast New Mexico and Application to Subsurface Reservoirs*. American Association of Petroleum Geologist: 27 pp.

Schlumberger. 2009. *Log Interpretation Charts 2009 Edition*: 268-270

Teklu, T.W., W. Alameri, H. Kazemi, and R.M. Graves. 2015. *Contact Angle Measurements on Conventional and Unconventional Reservoir Cores*. Unconventional Resources Technology Conference

Tonietto, S.N., M.Z. Smoot, and M. Pope. 2014. *Pore Type Characterization and Classification in Carbonate Reservoirs*. Geology and Geophysics, Texas A&M University.

Ruppel, S.C., and J. Kane. 2006. *The Mississippian Barnett Formation: A Source-Rock, Seal, and Reservoir Produced by Early Carboniferous Flooding of the Texas Craton*. Bureau of Economic Geology Jackson School of Geosciences, The University of Texas at Austin: 4 pp.

Wang, S., F. Javadpour, and Q. Feng. 2016. *Confinement Correction to Mercury Intrusion Capillary Pressure of Shale Nanopores*. Scientific Reports

Washburn, E.W. 1921. *The Dynamics of Capillary Pressure*. The Physical Review XVII.3

Webb, P.A. 2001. *An Introduction To The Physical Characterization of Materials by Mercury Intrusion Porosimetry with Emphasis On Reduction And Presentation of Experimental Data*. Micrometrics Instrument Corp.

Biographical Information

Griffin S. Mann is from Austin, Texas and graduated from Austin High School. He received his Bachelors of Science Degree in Geology from Texas Christian University in 2013. After working in the petroleum industry throughout his time at TCU and briefly after, he began pursuing a Masters of Science Degree in Petroleum Geoscience at the University of Texas at Arlington with an expected graduation in May of 2017. Throughout his time at UTA, Griffin has worked in the petroleum industry and intends to continue his work as a petroleum geologist after graduation.